BACHELOR THESIS
B. SC. IN PHYSICS

---

# Plasmon-driven chemistry: The role of particle size in the reduction of ferricyanide

---

Mareike Wübbenhorst

## UNIVERSITY OF POTSDAM

Institute of Physics and Astronomy
Ultrafast Dynamics in Condensed Matter

Examiner: Prof. Dr. Matias Bargheer
Co-Examiner: Prof. Dr. Ilko Bald

March 2022

Ich, Mareike Wübbenhorst, erkläre hiermit an Eides statt, dass ich die vorliegende Arbeit ohne Hilfe Dritter und ohne Benutzung anderer als der angegebenen Hilfsmittel angefertigt habe. Die aus fremden Quellen direkt oder indirekt übernommenen Gedanken und Abbildungen sind als solche kenntlich gemacht.

Ort, Datum Unterschrift

## Zusammenfassung

Die Photokatalyse mit Hilfe von Nanopartikeln eröffnet neue, kostengünstige Möglichkeiten, um chemische Reaktionen in Gang zu setzen, die normalerweise einen hohen Energieaufwand erfordern. Obwohl der Mechanismus vielversprechend erscheint, sind die bisher erreichten Wirkungsgrade leider nicht sehr ermutigend und die praktische Anwendbarkeit scheint noch fraglich. Um die Reaktionsgeschwindigkeit der Nanopartikel-gestützten Katalyse zu erhöhen, variiere ich in dieser Arbeit die Größe von mit Polivinylpyrrolidon (PVP) beschichteten Goldnanosphären zwischen 5 und 25 nm. Ich konnte Partikeln mit einer Größe von 10 nm eine maximale katalytische Fähigkeit zuordnen.

Die Erhöhung der Lösungstemperatur führte zu einer weiteren Steigerung der Reaktionsgeschwindigkeit, verändert aber gleichzeitig die Nanopartikel.

## Abstract

Photocatalysis using nanoparticles opens up new, cost-effective ways of initiating chemical reactions that generally require high energy input. Although the mechanism seems promising, the efficiencies achieved so far are unfortunately not very encouraging, and the practical applicability still seems questionable. To increase the reaction rate of nanoparticle-assisted catalysis, I varied the size of polyvinylpyrrolidone (PVP)-coated gold particles between 5 and 25 nm. I was able to assign a maximum catalytic ability to gold nanospheres with a size of 10 nm.

Increasing the solution temperature further increased the reaction rate, but at the same time changed the nanoparticles.

# Contents

# 1 Introduction

Within the last decades, the importance of nanoparticles has steadily increased in both basic research and applied science. Due to their promising ability to harness visible light for catalyzing chemical reactions, nanoparticles are expected to contribute to solving the currently pressing energy and resource problems [19]. For example, Yu et al. reported the possibility to use nanoparticles for the conversion of atmospheric $CO_2$ into liquid fuel under the influence of visible light [43]. However, it remains questionable whether the reaction efficiency can be increased to such an extent that it can prevail over existing processes.

A systematic understanding of the principles of reaction, as well as the influences of parameters such as material, size and shape, are crucial for increasing the efficiency of photocatalytic reactions [10].

In this work, I reproduced the experiments carried out by Kim et al. on the reduction of ferricyanide with different nanoparticle sizes to investigate the influence of particle size on the reaction rate [17].

In photocatalysis, the reaction kinetics are determined by the optical properties of the solution. Large nanoparticles not only absorb a different part of the optical spectrum, but they also scatter a large fraction of the incident light [33]. For the energy provided by the laser light to be optimally absorbed, I had to use small particles for the experiments and the nanoparticles in one sample were required to be of the same size. However, the fabrication of small nanoparticles with a narrow size distribution is particularly challenging [30], so the fabrication process and underlying mechanisms are given considerable attention in this work.

As highly concentrated nanoparticle solutions absorbs a greater proportion of incident light than a solution of lower concentration, I had to pay special attention to the adjustment of the particle concentration.

Also, a higher reaction temperature might accelerate the reaction, so a focus on the effect of temperature on the reaction rate is important.

I prepared eight nanoparticle samples with sizes ranging from 5 to 22 nm, following a recipe described by Piella et al. [29] and coated them with polyvinylpyrrolidone (PVP). The nanoparticle size and size dispersion could be determined from TEM images. To adjust the concentrations of the particles, I had to centrifuge the solutions, which was not possible for all samples due to the low particle mass. Using the intensity observations from the UV-Vis spectroscopy data, I could calculate the reaction rates for the different samples.

My results suggest that two size-dependent mechanisms significantly affect the reaction rate: Due to the increasing surface-to-volume ratio with decreasing radius, the surface area available for catalysis increases, and small nanoparticles tend to catalyze chemical reactions better. At the same time, the hot-carrier generation becomes maximally efficient at a size of 10 nm and thus enables particularly high reaction rates.

I have found that catalysis is greatly enhanced by increased reaction temperatures, even in the dark. Especially at high reaction temperatures, the nanoparticles also undergo a chemical reaction.

# 2 Theoretical Background

This section first addresses the conditions that facilitate the synthesis of small and monodisperse nanoparticles with long-term stability and minimal diameter variations.The principles underlying the photocatalytic reactions supported by nanoparticles are then described, and the properties of the light-matter interaction of nanoparticles are briefly discussed.

## 2.1 Principles of Colloid Formation

The history of nanoparticles dates back to Roman times, when traces of precious metals have first been incorporated in artistic glasswork during the manufacturing process [23]. Also, in the Middle Ages, glass mixed with nanoparticles was used to furnish church windows with colorful images [19, 25]. In the 19th century, Michael Faraday was the first to succeed in synthesizing colloidal gold in solution by making a gold salt react with white phosphorus [19, 30]. Various techniques have been developed to prepare gold nanoparticles of different sizes and shapes, most of which are based on a reaction developed by Turkevich in 1950. In this recipe, trisodium citrate is used as a reducing agent to decompose gold hydrochloride ($HAuCl_4$) into its components to produce gold ions in solution, which subsequently self-assemble and grow into nanoparticles [39]. All chemical approaches to nanoparticle formation consist of several steps that interlock and influence each other - the formation of initial nuclei, growth process and particle stabilization - making it challenging to develop a comprehensive explanatory approach [30].

Jörg Polte's summary paper 'Fundamental growth principles of colloidal metal nanoparticles – a new perspective' [30] brings together all previous findings on reaction and growth processes to develop different description attempts that may be helpful for practical application.

### 2.1.1 Nucleation

Becker and Doring were the first to attempt a thermodynamical description of the processes and principles of nanoparticle fabrication in the 1930ies. Their so-called Classical Nucleation Theory (CNT) [3] initially described the phase transition from vapor to liquid. Later it was extended to other phase transitions, including crystallization processes [30]. This theory is based on the principle of the minimization of Gibb's free energy using macroscopic parameters.

The Gibb's free energy of spherical nuclei spontaneously forming in a solution (**homogeneous nucleation**) is given by formula (1) and strongly depends on their particle radius [30, 31].

$$\Delta G = 4\pi r^2\gamma - \frac{4}{3}\pi r^3|\Delta G_V| \tag{1}$$

where:
$\Delta G$: total change in Gibb's free energy
$r$: radius of the nucleus
$\gamma$: surface energy per unit area
$\Delta G_V$: change in Gibb's free energy per unit volume

This expression (as displayed in figure (1a)) reaches a maximum at a critical radius $r^*$ where the nanoparticle becomes stable. Nuclei formed at a size below $r^*$ dissolve to minimize Gibb's free energy, whereas for particles with a radius above $r^*$ growth is more favorable. [19, 30]

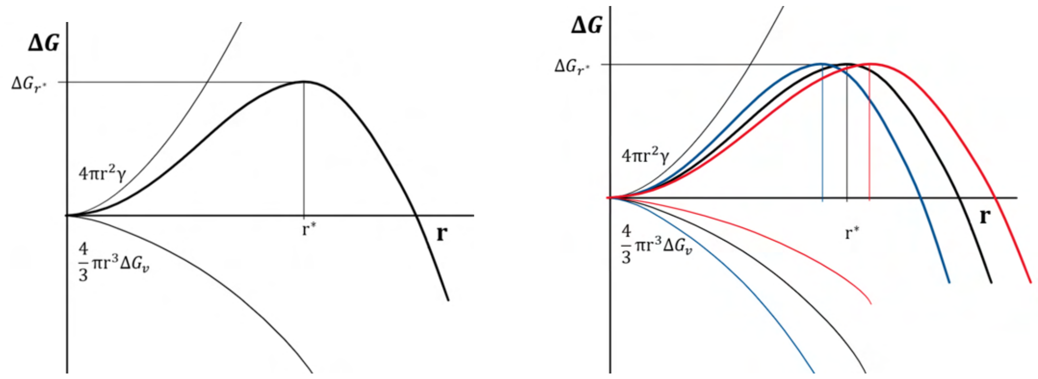

(a) $\Delta G$ dependent on particle radius $r$

(b) $\Delta G$ for different temperatures $T$

Figure 1: Gibb's free energy $\Delta G$

The critical radius can be easily derived from $\frac{d\Delta G}{dr} = 0$ which leads to:

$$r^* = \frac{2\gamma}{|\Delta G_V|} \tag{2}$$

When considering the temperature dependence of the particle formation process, the change in Gibb's free energy per unit volume $\Delta G_V$ can be expressed as

$$\Delta G_V = \frac{H_V \cdot (T - T_m)}{T_m}$$

where:
$\Delta G_V$: change Gibb's free energy per unit volume
$H_V$: heat of fusion per unit volume (enthalpy)
$T$: temperature of solution
$T_m$: melting temperature of the solid
[19, 28]

Assuming $H_V$, $T_m$ and the surface tension $\gamma$ remain constant, we get different graphs of $\Delta G$ for different temperatures $T_1 < T_2 < T_3$ from formula (1) as

shown in figure (1b).
The critical radius $r^*$ can now be expressed as

$$r^* = \frac{2\gamma \cdot T_m}{|H_V \cdot (T - T_m)|}$$

Thus, $r^*$ also increases with temperature (cf. figure 1b).

Following this description, heating the reaction solution more strongly leads to a higher value of the critical radius. Smaller nuclei with a radius below $r^*$ cannot remain stable and dissolve during the nanoparticle formation process, leading to a higher polydispersity of the resulting solution.
*Thus, a comparably low temperature may be favorable to the synthesis of a monodisperse nanoparticle solution.*
The effective surface energy $\gamma$ is reduced on impurities in solution or surfaces of glassware or laboratory gear, leading to the preferential formation of nuclei (**heterogeneous nucleation**). This leads to the assumption that even though both processes are needed for the successful synthesis of nanoparticles, heterogeneous nucleation can be seen as the 'driving force' [30] in seed-mediated nanoparticle fabrication.
Most of today's theoretical work is still based on CNT, although its predictions are not very reliable. This theory only describes the nucleation process but fails to describe growth and neglects stabilization mechanisms. [30]

### 2.1.2 Growth

The LaMer model is based on the principle of supersaturation and adds a rudimentary explanation of the growth process to the description of nanoparticle formation. This more chemically oriented approach was initially developed to describe the formation of sulfur colloids in an ethanol-water mixture: Sulfur is highly soluble in ethanol but not in water. As water is added to a sulfur-ethanol solution, the solubility of sulfur gradually decreases. After reaching a critical saturation, nuclei form spontaneously in the solution lowering the saturation level. [20, 21]

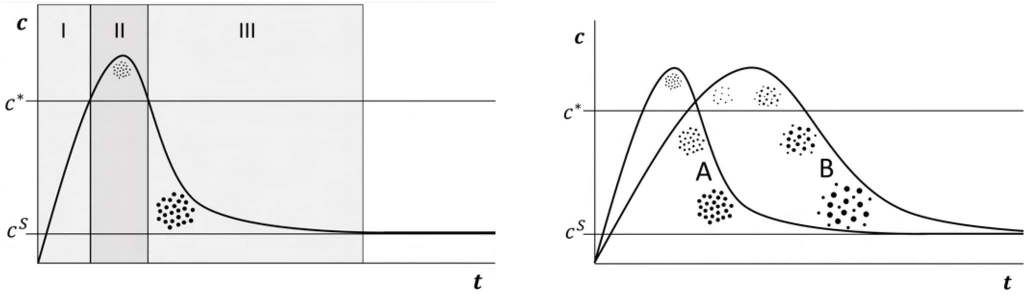

(a) Three phases of collodial formation:
**I**: Reduction of precursor
**II**: Formation of initial nuclei
**III**: Growth

(b) **A**: Strong reducing agent leading to small, monodisperse particles
**B**: Weak reducing agent leading to a solution of polydisperse particles

Figure 2: LaMer model of collodial formation

Figure (2a) shows a general LaMer process as a function of time. In the case of noble metal colloids, supersaturation is achieved by adding a reducing agent to isolate the metal ions from the salt compound. The vertical axis shows the total nanoparticle concentration, with free ions counted as monatomic particles. The salt is more soluble in water than the ions, so the concentration quickly reaches a critical value $c^*$ (**I**). As long as the particle concentration remains above $c^*$, nuclei are formed everywhere in the solution (**II**), which immediately begin to grow on freshly reduced free ions. The formation and growth of these initial nanoparticles reduce the total particle concentration in the solution until a saturation $c^S$ is reached (**III**).

Based on these considerations, different scenarios are imaginable (cf. (2b)): A short nucleation phase favors the synthesis of monodisperse nanoparticle solutions. The nuclei are formed almost simultaneously, and all particles have the same conditions for their growth process (**A**). In such a fast reduction process, reduction and growth can be considered separately.

On the other hand, if the reduction process is slow, nucleation can occur while the reduction is still in progress: the nucleation period and growth period overlap. Some nanoparticles have more time to grow before all metal ions are consumed (**B**). [19, 29, 30]

*In conclusion, a stronger reducing agent, inducing a quicker reaction, works in favor of a high monodispersity of the nanoparticle solutions.*

The LaMer model gives an idea of the general nucleation and growth process of colloids. However, in the case of metal nanoparticles, the description is still insufficient. Most importantly, the stability of the resulting particles remains unmentioned, although, for most recipes, the role of a capping agent for stabilization is essential. Therefore, for a better understanding of the growth kinetics of nanoparticle synthesis, colloidal stability must be included in the colloid formation model.

### 2.1.3 Stabilization

Without a stabilizing component (the ‘capping agent’), nanoparticle stability is governed by two opposite potentials: The attractive Van der Waals Potential, which for two identical particles can be simplified to a distance dependence of $\sim \frac{1}{d^6}$ [19], and the electrostatic repulsion, which essentially depends on the chemical properties of the solution.
The total interaction potential $W$ can then be described as the sum of the two potentials and can be plotted in dependence of the interparticle distance $a$ (as shown in figure (3a)). The curve's maximum (the ‘aggregation barrier’ $W^*$) can be interpreted as an activation energy that must be overcome to form a cluster. The aggregation barrier increases with increasing radii as can be seen in figure (3b) [30].

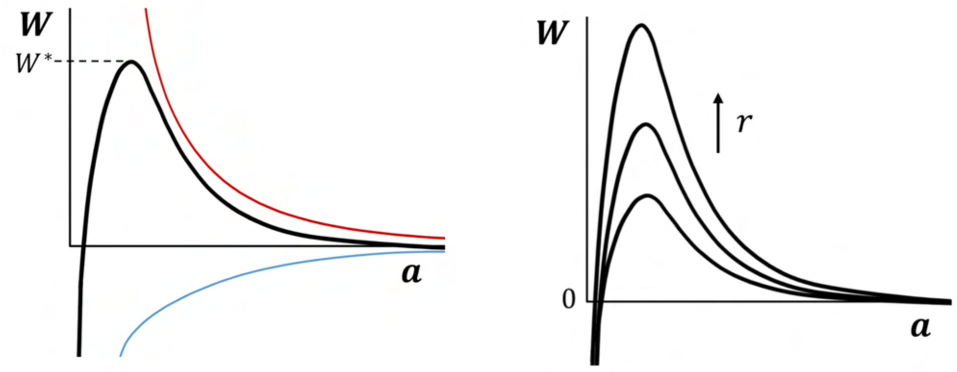

(a) $W$ as a sum of Van der Waals potential and electrostatic potential

(b) $W$ for different radii $r$

Figure 3: total potential $W$ in dependence of the interparticle distance $a$ of two identical nanoparticles

What ultimately determines the stability is the thermal energy $W_{kT}$ of the nanoparticles. For smaller radii, coagulation into larger particles is energetically favorable as a given thermal energy $W_{kT}$ easily overcomes the corresponding comparably low aggregation barrier (see section ‘growth’ in figure (4)). As $W^*$ increases with size, thermal energy might not be sufficient to overcome the aggregation barrier, and the particles remain stable after reaching a critical radius $r^*$ (‘stable particles’ in figure (4)). However, if $W_{kT}$ is too high, coagulation remains energetically useful for the nanoparticles until the particles coagulate (‘coagulation’ in figure (4)). [30].

*The model suggests that to produce small nanoparticles, a high reaction temperature and thus high thermal energy* $W_{kT}$ *may be disadvantageous*

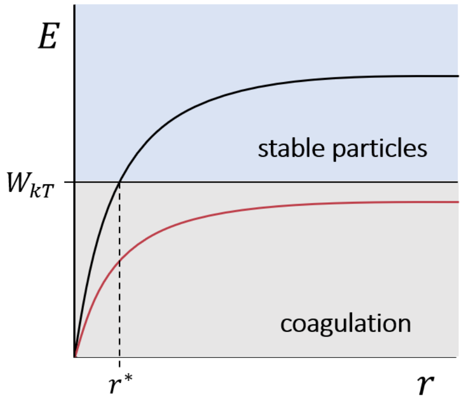

Figure 4: Possible paths of growth depending on the thermal energy $W_{kT}$ (cf. [30]

Based on these results, two different explanatory models of growth processes can be distinguished:

**Category 1**

If the reducing agent is strong enough, the clustering of ions into initial nuclei can be described to happen instantaneously. As long as the radii of the nanoparticles remain below $r^*$, the nuclei coalesce into larger nanoparticles (cf. figure (5)). Whether and when this coagulation process is stopped depends on the strength of the stabilizing agent and the temperature of the solution.

**Category 2**

A weaker reducing agent produces only a small amount of gold ions in the first stage of the process. During the reduction procedure, new gold ions can adsorb onto the initial clusters and lead to a so-called 'diffusional growth' (cf. figure (6)). The growth process stops as soon as all material is consumed, but coalescence of two clusters into larger particles can still be possible [30].

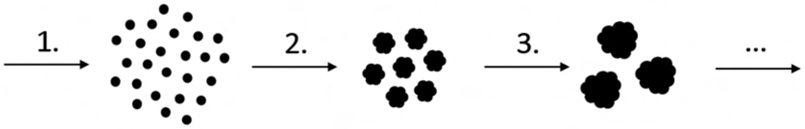

Figure 5: **Category 1**: Reaction process with a strong reducing agent
**1.** Fast reduction of precursor
**2.** Initial clustering
**3.** Coalescence into larger particles

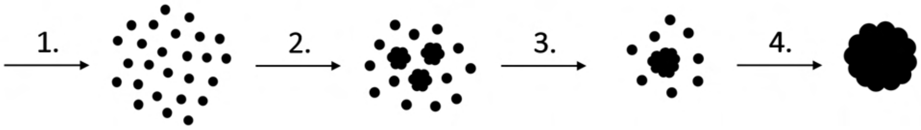

Figure 6: **Category 2**: Reaction process with a weak reducing agent
**1.** Reduction of precursor
**2.** Initial clustering while more material reacts
**3. & 4.** Coalescence and diffusional growth into larger particles

*A fast reduction of the precursor enabled by the use of a strong reducing agent can lead to a fast and controlled clustering process. Reduction, nucleation and growth do not interfere too much so that all particles find the same basic conditions and a high monodispersity can be achieved. At low reaction temperatures and in the presence of a capping agent, the particles can already stabilize at a small size.*

## 2.2 Plasmon-driven Catalysis

An external electric field can cause the electrons in a nanoparticle to be dislocated from their atomic core (cf. figure 7a)). When the frequency of an incident photon matches the natural frequency of the electron cloud, a collective oscillation of the electron cloud occurs, known as LSPR ('Localized Plasmon Resonance') [1].

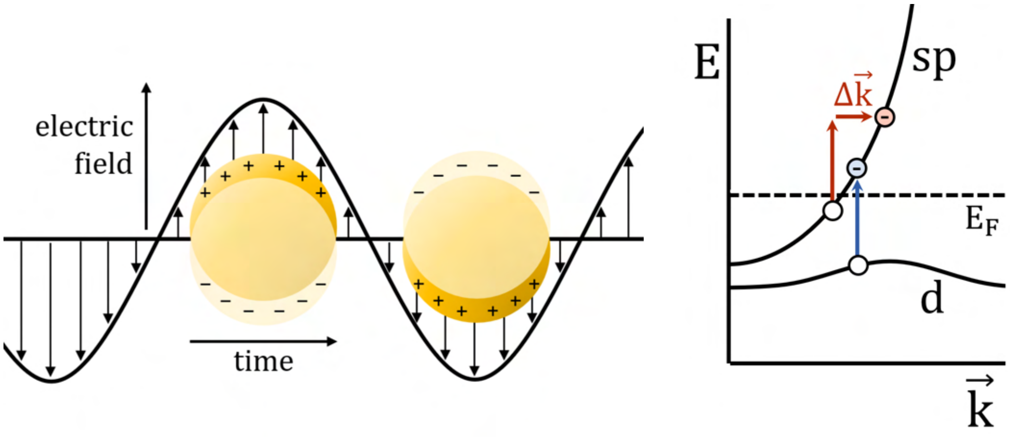

(a) (b)

Figure 7: **(a)** Interaction of the nanoparticle with the electric field of incident light (cf. [33])
**(b)** Interband (blue) and intraband transitions (red) in a simplified band structure diagram

A nanoparticle can either immediately re-emit the absorbed photon into the far-field ('radiative decay') or transfer the extra energy to charge carriers within the nanoparticle ('non-radiative decay'), allowing the electrons to change their position within the band structure of the metal [1, 43].
These band transitions can only occur to allowed states, that can be visualized by a dispersion relation (cf. figure (7b)). If an electron is excited in the sp-band, it must scatter at an impurity such as the particle surface in order to receive an additional momentum ($\Delta\vec{k}$) and thus return to an allowed state

(indirect intraband transition) [5]. Unlike in silver or copper, the d-band in gold is located just below the Fermi energy $E_F$, so that direct intermediate band transitions into unoccupied states of the sp-band can be excited by visible light [1, 2]. These so-called 'hot charge carriers', instead of recombining within the nanoparticle, can then be transferred to neighboring molecules to induce a chemical reaction [43].

The one-electron reduction of the center iron-ion $\mathrm{Fe}^{3+}$ of ferricyanide $\left(\mathrm{Fe(CN)}_6\right)^{3-}$ to $\mathrm{Fe}^{2+}$ of ferrocyanide $\left(\mathrm{Fe(CN)}_6\right)^{4-}$ has been extensively studied due to its simplicity [6, 14]. In the procedure described by Kim et al., ferricyanide is added to a nanoparticle solution and excited with high-intensity CW laser light near the plasmon resonance of the particles. The solution is continuously stirred to allow quasi-uniform exposure to light [17].

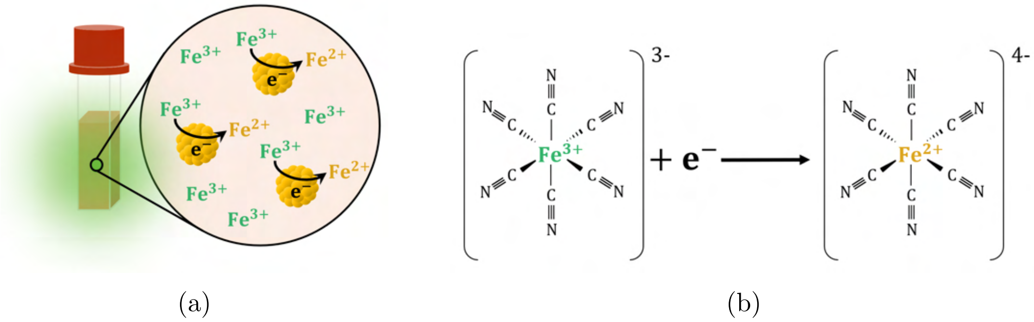

(a) (b)

Figure 8: Reaction mechanism **(a)** and molecular structure **(b)** of the light-induced reduction of ferricyanide ($\mathrm{Fe}^{3+}$) to ferrocyanide ($\mathrm{Fe}^{2+}$).

When excited by light, the gold nanoparticles are assumed to transfer electrons to neighboring ferricyanide molecules and reduce them to ferrocyanide (cf. figure (8)) [16].

This charge transfer requires a counter reaction that provides electrons to the reaction process. For example, water can oxidate by forming an OH radical ($\bullet\,\mathrm{OH}$), thus acting as a 'hole scavenger'[17, 32]:

$$\mathrm{H_2O} \rightarrow \bullet\,\mathrm{OH} + \mathrm{H}^+ + \mathrm{e}^-$$

As water has a comparably high oxidation potential, the oxidation proceeds very slowly. After a short time, the nanoparticles can no longer supply electrons and the reaction rate reaches saturation [17]. The addition of a substance with a lower oxidation potential, such as ethanol, can help to overcome this effect by more efficiently providing electrons for the nanoparticles [17, 43].

By the oxidation of Ethanol ($C_2H_5OH$) to a Hydroxyethyl radical ($C_2H_5O\bullet$), one electron is provided by the following reaction:

$$\mathrm{C_2H_5OH + h^+ \rightarrow C_2H_5O\ \bullet + H^+}$$

For higher laser power and an associated increase in the need for hole-scavenging, the Hydroxyethyl radical can react to Acetaldehyde (Acetaldehyde), providing a second electron for the reduction of $Fe^{3+}$.

$$\mathrm{C_2H_5O\ \bullet + h^+ \rightarrow CH_3CHO + H^+}$$

Increasing the Ethanol concentration further raises the reaction rate until it reaches saturation as soon as the charge transfer becomes rate-limiting - which, according to experience, is only the case above a concentration of $c_{\mathrm{EtOH}} \sim 10c_{\mathrm{Fe}^{3+}}$ [17]. Based on the experiments described by Kim et al., adjusting the ethanol concentration to a value between 0.5 M and 3 M seems reasonable for successful photocatalysis.

During the reaction under aerobic conditions, oxygen dissolved in the water may absorb electrons provided by the nanoparticles to reach the noble gas state. This can be avoided by purging the solution with nitrogen gas to remove oxygen from the solution. Ethanol must be added after deoxygenation to prevent evaporation.

# 3 Methods

Both the nanoparticles and the reaction components have the pleasant property of interacting with visible light, so the reaction kinetics can be detected using UV-Vis spectroscopy, and more complicated analytical techniques such as mass spectroscopy are not necessary. The method for determining the conversion rate from the spectra is essentially based on the calculations described by Kim et al. [17].

## 3.1 UV-Vis Spectroscopy

The interaction of light and matter can be observed by determining the fraction of a given light intensity that passes through a sample and reaches the detector behind it. In physics, the term 'extinction' describes the totality of light that is not transmitted. Despite the risk of confusion with the term 'absorption', the same fraction of light is often referred to as the 'absorbance' in a chemical context and will also be used in this work to align with the terminology used by Kim et al. [17]. The only difference in calculation between the two conventions is the use of the logarithm to base ten as opposed to the base of Euler's number in Lambert-Beer's law [33]:

$$\mathrm{Ext}_\lambda = ln\Big(\frac{I_0}{I}\Big) = \epsilon_\lambda \cdot c \cdot d \tag{3}$$

$$\mathrm{Abs}_\lambda = log_{10}\Big(\frac{I_0}{I}\Big) = \alpha_\lambda \cdot c \cdot d \tag{4}$$

where:
$\mathrm{Ext}_\lambda$, $\mathrm{Abs}_\lambda$: Extinction and Absorbance of the sample at wavelength $\lambda$
$I_0$: intensity of the incident beam [%], $I_0 = 100\%$
$I$: intensity of the transmitted beam [%], $I =$ recorded spectrum
$\epsilon_\lambda$, $\alpha_\lambda$: Extinction and Absorbance coefficient at wavelength $\lambda$ $[\frac{1}{\mathrm{M \cdot cm}}]$
$c$: concentration of the sample $[\mathrm{M} = \frac{\mathrm{mol}}{\mathrm{l}}]$
$d$: thickness of cell [cm]

The light that does not reach the detector may have been reflected, scattered or absorbed by the sample. The contributions of scattering and absorption can be best described by looking at the proportions of their cross sections as the total cross section (absorbance or extinction) results from the sum of the two components:

$$\sigma = \sigma_{abs} + \sigma_{scat}$$

Due to the small size, spherical shape and high conductivity of the nanoparticles used in this work, a dipole approximation can be used to describe their interaction with light [33]. The polarizability of a nanoparticle $\alpha$ is then given by:

$$\alpha = 4\pi\varepsilon_0 r^3 \frac{\varepsilon_{sph} - \varepsilon_{med}}{\varepsilon_{sph} + 2\varepsilon_{med}} \tag{5}$$

where:
$r$: radius of the spherical nanoparticle
$\varepsilon_0 = 8.85 \cdot 10^{-12} \frac{\mathrm{A \cdot s}}{\mathrm{V \cdot m}}$: electrical field constant
$\varepsilon_{sph}$: permittivity of the sphere
$\varepsilon_{med}$: permittivity of the medium

which can be used to calculate the absorption cross section $\sigma_{abs}$ and the scattering cross section $\sigma_{scatter}$ as follows:

$$\sigma_{abs} = \frac{k}{\varepsilon_0} Im[\alpha] \quad \text{and} \quad \sigma_{scat} = \frac{k^4}{6\pi\varepsilon_0^2}|\alpha|^2$$

where:
$k = \frac{2\pi}{\lambda}$: wave vector

And we get

$$\sigma_{abs} = 4\pi k r^3 Im\left[\frac{\varepsilon_{sph} - \varepsilon_{med}}{\varepsilon_{sph} + 2\varepsilon_{med}}\right] \quad \text{and} \quad \sigma_{scat} = \frac{8\pi k^4 r^6}{3}\left|\frac{\varepsilon_{sph} - \varepsilon_{med}}{\varepsilon_{sph} + 2\varepsilon_{med}}\right|^2 \tag{6}$$

In table (1) the scattering and absorption cross sections with the respective quotients are calculated for five exemplary nanoparticle sizes. The nanoparticles are excited with a laser at wavelength $\lambda = 532$ nm and we can assume $\varepsilon_{sph} = 2 + 3.7i$ for gold and $\varepsilon_{med} = 1$ for water. [33]

| $r$ **in nm** | $\sigma_{abs}$ **in nm**$^2$ | $\sigma_{scat}$ **in nm**$^2$ | $\frac{\sigma_{scat}}{\sigma_{abs}}$ **in %** |
|---|---|---|---|
| 2.5 | 0.87 | 0.00002 | 0.002 |
| 5 | 6.9 | 0.001 | 0.02 |
| 10 | 187.3 | 0.92 | 0.49 |
| 15 | 443.9 | 5.2 | 1.16 |

Table 1: Absorption cross sections $\sigma_{abs}$ and scattering cross sections $\sigma_{scat}$ calculated for different radii $r$ using formula (6)

The nanoparticles absorb most strongly the LSPR, which can be observed as an isolated peak in spectroscopy. Since the plasmon resonance is size and morphology dependent, observing the LSPR peak in UV-Vis spectroscopy allows a first estimation of the nanoparticle size. For a diameter below 50 nm the absorbance maximum shifts toward higher energies and becomes increasingly flat and broad as the size of the nanoparticles decreases [13, 15, 24, 29].

## 3.2 Determinantion of the Reaction Rates

Figure (9a) shows the spectra of the mixture of nanoparticles, ethanol and the molecules $Fe^{3+}$ and $Fe^{2+}$ during the reaction process. While the absorbance peak caused by ferricyanide ($Fe^{3+}$) decreases with time, the absorbance caused by ferrocyanide ($Fe^{2+}$) increases, indicating a change in the composition of the solution and, thus, successful catalysis. In order to evaluate the data quantitatively, some corrections are necessary.

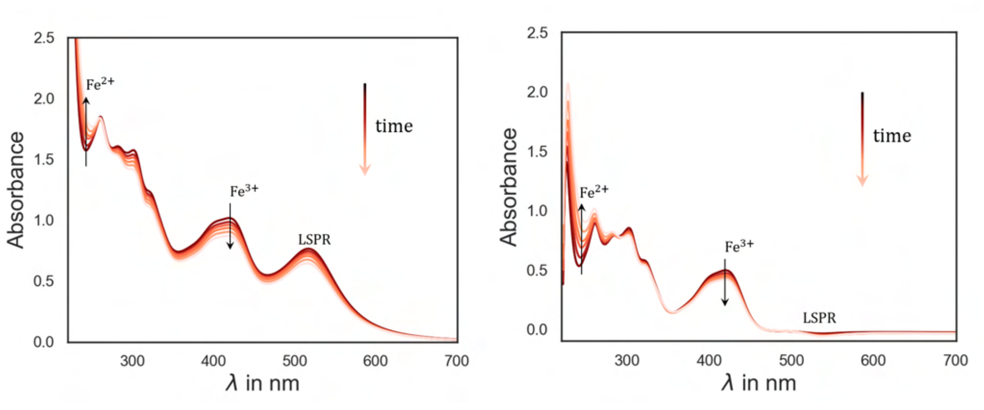

(a) (b) corrected spectrum

Figure 9: Reaction kinetics of $Fe^{3+}$ to $Fe^{2+}$ observable in UV-Vis spectroscopy at 55 °C

First, the absorbance of the nanoparticles must be removed from the spectrum by applying the following calculation to each spectrum:

$$\text{Spectrum}_{\text{corrected}} = \text{Spectrum}_{\text{Sample}} - \frac{\text{Peak Absorbance}_{\text{Sample}}}{\text{Peak Absorbance}_{\text{AuNS}}} \cdot \text{Spectrum}_{\text{AuNS}} \tag{7}$$

The **Peak Absorbance** is the difference between the maximum absorbance and the sample absorbance at 800 nm, where the reaction solution does not interact with light.

As the spectrum of $Fe^{3+}$ shows an absorbance onset at 465 nm, the corrected spectra must be shifted so that the absorbance at 465 nm is zero (cf. figure (9b)).

$$\text{Spectrum}_{\text{corrected}} = \text{Spectrum}_{\text{Sample}} - \text{Value}_{\text{Sample}}(465\ \text{nm})$$

To determine the concentration changes of $Fe^{3+}$ and $Fe^{2+}$, the absorbance coefficient $\alpha_\lambda$ must be determined for both molecules. The molecules are diluted in water and UV-Vis spectroscopy is carried out (cf. figure(10)). Although $Fe^{2+}$ shows its maximum absorbance at 218 nm, the change in concentration can be best observed at 240 nm, where $Fe^{2+}$ shows a minimum in absorbance. The concentration change of $Fe^{3+}$ will be observed at a wavelength of $\lambda = 419$ nm where $Fe^{2+}$ shows no absorbance in UV-Vis-spectroscopy.

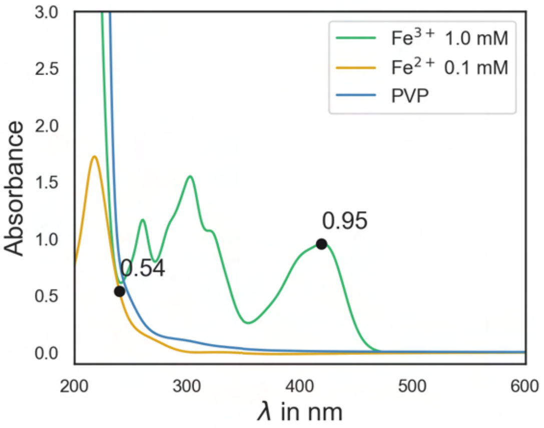

Figure 10: Absorbance spectra of $Fe^{3+}$, $Fe^{2+}$ and PVP in $H_2O$ in a cuvette of $d = 1$ cm
black dots indicate absorbance values $Abs_\lambda$ at $\lambda = 240$ nm of $Fe^{2+}$ and $\lambda = 419$ nm of $Fe^{3+}$

With the help of Lambert-Beert's law (see formula (4)) the absorbance coefficients can be calculated using formula:

$$\alpha_\lambda = \frac{Abs_\lambda}{c \cdot 1\,\mathrm{cm}} \tag{8}$$

And we get $\alpha_{240\text{ nm}} = 5400 \frac{1}{\mathrm{M}\cdot\ \mathrm{cm}}$ and $\alpha_{419\text{ nm}} = 950 \frac{1}{\mathrm{M}\cdot\ \mathrm{cm}}$.
The ratio $\frac{\alpha_{240\text{ nm}}}{\alpha_{240\text{ nm}}} = 5.684$ deviates by 4.7 % from the value used in the paper of Kim et al. [17].
The concentration changes can now be calculated by deviding the change in absorbance of the corresponding wavelengths over time by the associated absorbance coefficient:

$$\mathrm{conv}(t) = \frac{\mathrm{Abs}_\lambda(t) - \mathrm{Abs}_\lambda(t=0)}{\alpha_\lambda} \tag{9}$$

where:
$[conv] = \ \mathrm{M}\cdot\ \mathrm{cm}$
Since the cuvette has a length of one centimeter, the conversion can be given in moles per liter (M).
Looking at the curves shown in figure (10), a decrease in the absorption peak at 419 nm along with a decrease in the concentration of $\mathrm{Fe}^{3+}$ would be unaffected by any change in the concentration of $\mathrm{Fe}^{2+}$. The increase in the concentration of $\mathrm{Fe}^{2+}$ (visible at 240 nm), however, overlaps with the simultaneous decrease in the absorbance of $\mathrm{Fe}^{3+}$ at the same wavelength. Also, the red-shift of the $\mathrm{Fe}^{2+}$ absorbance minimum in figure (9b) indicates that absorbance values taken at 240 nm may not reflect the conversion correctly. The conversions of $\mathrm{Fe}^{3+}$ and $\mathrm{Fe}^{2+}$ calculated with the help of the calculated absorbance coefficients show different trends (cf. figure (11)).
The contribution of nanoparticle absorption is removed for each spectrum separately. Therefore, the decrease in absorbance at 419 nm translates into a decrease in $\mathrm{Fe}^{3+}$ concentration, which in turn must be accompanied by an increase in $\mathrm{Fe}^{2+}$ concentration since no material is lost in this process. It

is therefore justifiable that the best estimation for conversion calculations is based on the observations at wavelength $\lambda = 419$ nm which will be used in the following to quantify the conversion of $Fe^{3+}$ to $Fe^{2+}$.

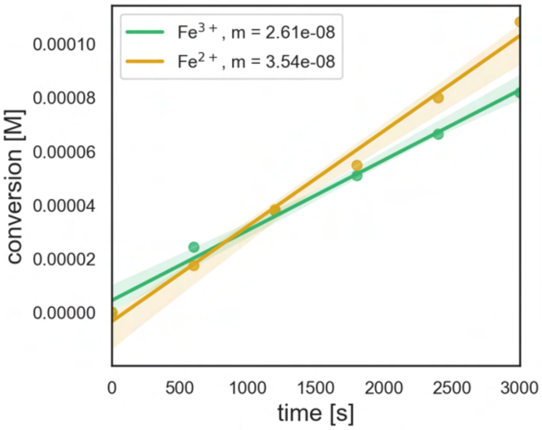

Figure 11: Calculated conversion of $Fe^{3+}$ and $Fe^{2+}$ for figure (9)
The reaction rate $K$ corresponds to the slope of the linear fit $m$

At this wavelength, it is also impossible for residual PVP remaining in the solution to influence the spectroscopic data. As can be seen in figure (10), PVP only begins to absorb at about 350 nm.

# 4 Experimental Results

Based on the calculations presented in table (1), only nanoparticles with a radius below 15 nm will be used in this work to minimize the scattering cross-section. For stabilization, the particles are coated with a polymer before being used for catalysis. Some additional measurements are necessary to minimize the influences of concentration and temperature before it can be determined to what extent the reaction rate depends on the size of the nanoparticles.

## 4.1 Preparation of Nanoparticles

The recipe that is most commonly used for the preparation of citrate-stabilized gold nanoparticles has been described by Turkevich [39] and extended by Frens [9] and cannot be used for the preparation of small nanoparticles (< 10 nm) [29]. Following the assumptions described in section 'Colloid Formation', this might be explained by the fact that the recipe uses a comparably weak reducing agent and high reaction temperature.

Piella et al. succeeded in creating nanoparticles with a size of a few nanometers by adding a small amount of the strong reducing agent tannic acid, allowing the explosive formation of gold nuclei [29]. The excellent stabilizing properties of sodium citrate combined with a comparably low reaction temperature of 70 °C increase the monodispersity and stability of the small colloids [30]. In a second step, reactants are again added to the solution so the nanoparticles can grow to the desired size.

For the synthesis of the nanoparticles used in the catalysis experiments, I essentially followed the recipe of Piella et al., but omitted the addition of potassium carbonate, which would have led to a minor reduction in size [29]. This approach offers the advantage that the different sizes are synthesized one after the other in a single recipe. In this way, unpredictable variations in the manufacturing requirements are minimized.

I synthesized the nanoparticles in a 250 ml three-neck flask, heated by a heating mantle from the outside. To avoid evaporation of the solution, I used a water-cooled condenser and controlled the solution temperature with the help of a glass-covered temperature sensor. The chemicals used were ordered from Sigma Aldrich. CHEMICALS

- Sodium citrate tribasic dihydrate, 2.2 mM in $H_2O$
- tannic acid, 2.5 mM in $H_2O$
- $HAuCL_4$, 25 mM in $H_2O$

SYNTHESIS OF 5 NM SEEDS (AUNS 0) I heated 75 ml of 2.2 mM sodium citrate with 50 $\mu$l of 2.5 mM tannic acid under continuous stirring at 800 rpm. As soon as the solution reached 70 °C, I added 500 $\mu$l of 25 mM $HAuCl_4$. The solution color immediately changed to black, then slowly turned into brownish-orange within two minutes. I kept the solution at 70 °C for five minutes to ensure the complete reaction of the components. I then extracted 27.5 ml of solution with a glass pipette and allowed the solution to cool in the refrigerator.

GROWTH INTO LARGER PARTICLES (AUNS 1-7) (CF. APPENDIX **A**)

To let the nanoparticles grow, I had to add additional reaction products to the solution.

First, I replaced the extracted nanoparticle solution with 27.5 ml of 2.2 mM sodium citrate and waited until the solution reached 70 °C again. After the subsequent addition of 250 $\mu$l of 25 mM $HAuCl_4$, the solution color changed to dark purple and slowly turned red. To ensure a complete reaction, I waited ten minutes before injecting another 250 $\mu$l 25 mM $HAuCl_4$. After ten minutes, I removed 27.5 ml of the solution and placed it in the refrigerator. By repeating these steps, I obtained eight nanoparticle solutions.

The increase in particle size in each growth step is visible to the bare eye (cf. figure (12)) and can be observed by UV-Vis spectroscopy (cf. figure (13)).

Figure 12: Photography of the nanoparticle samples after seven growth-steps

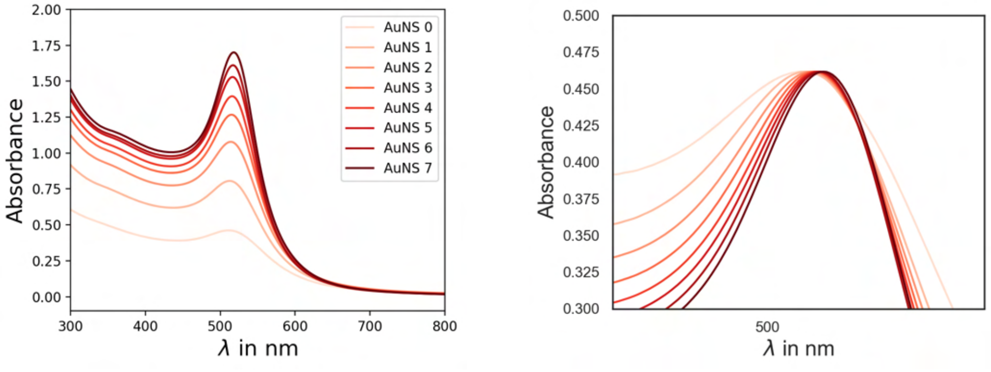

(a)

(b)

Figure 13: **(a)** Spectra of the nanoparticle samples after seven growth-steps **(b)** Section of the spectra normalized to the LSPR peak

The plasmon resonance above 500 nm steadily increases (cf. figure (13a)) with particle size, accompanied by a red-shift of the plasmon peak that can be made visible by normalizing the peaks of the LSPR band to an arbitrary height (cf. figure (13b)). With each growth step, the number of available electrons per particle increases, which amplifies and shifts the resonance conditions of the electron cloud [13].

Using the image processing program IMAGEJ, I measured the individual particles from TEM images kindly performed by Radwan Mohamed Sarhan at Helmholtz-Zentrum Berlin (HZB) (14). The data recorded in this way are shown in the histogram in figure (15), the associated mean values and standard deviations are listed in the table (2).

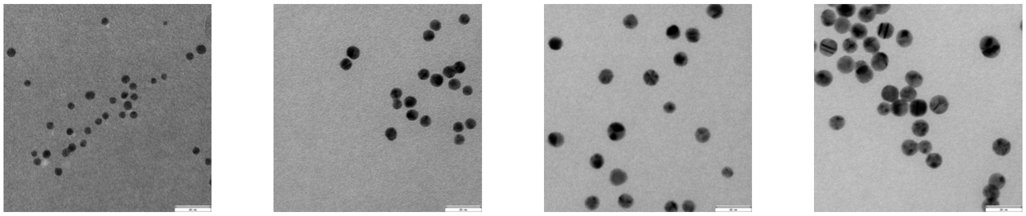

(a) AuNS 0 (b) AuNS 1 (c) AuNS 2 (d) AuNS 3

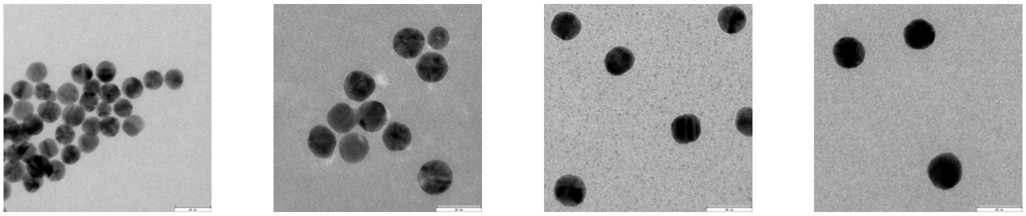

(e) AuNS 4 (f) AuNS 5 (g) AuNS 6 (h) AuNS 7

Figure 14: TEM images of 'AuNS 0-7'

The diameters of the spherical gold nanoparticles range from 5 to 22 nm with an average size variation of 11.4 %. As the number of nanoparticles decreases due to the design of the recipe (explained in more detail in appendix **B**), the larger samples grow more than the smaller ones.

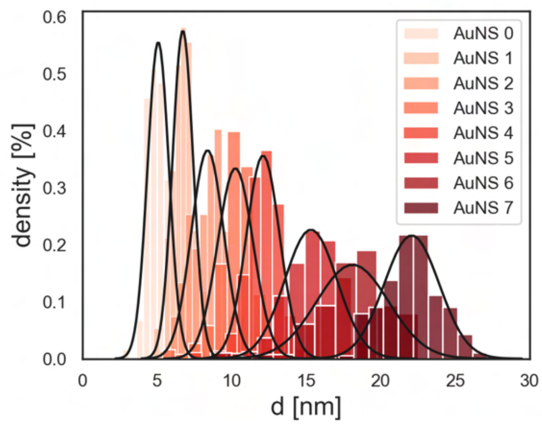

Figure 15: Histogram of particle sizes present in each solution with associated Gaussian fits

| **AuNS** | $\bar{d}$ **[nm]** | $\sigma$ **[nm]** | $\sigma$ **[%]** |
|---|---|---|---|
| **0** | 5.09 | 0.72 | 14.1 |
| **1** | 6.74 | 0.69 | 10.3 |
| **2** | 8.40 | 1.09 | 12.9 |
| **3** | 10.26 | 1.19 | 11.6 |
| **4** | 12.11 | 1.12 | 9.2 |
| **5** | 15.33 | 1.76 | 11.5 |
| **6** | 18.13 | 2.41 | 13.3 |
| **7** | 22.09 | 1.84 | 8.3 |

Table 2: Mean diameter $\bar{d}$ and standard deviation $\sigma$ as determined from the Gaussian distributions shown in figure (15)

### 4.1.1 Functionalization

The citrate bound to the surface of the gold nanoparticles during the fabrication process can be easily exchanged due to its low binding strength [29]. In the procedure described by Yu et al., the ligand exchange from citrate to PVP takes place under ultrasonic treatment [42].

PVP is known to be stable under photocatalytic reactions [42] while not affecting the catalytic properties of the nanogold [12, 37]. Furthermore, in comparison to the citrate, which protects the nanoparticles by electrostatic repulsion, PVP stabilizes the nanoparticle by simply acting as a spacer between the particles [22, 31]. The molecule consists of an unbranched (linear) polymer chain (cf. figure (16)), which is commercially available in various lengths, that vary by their molar masses.

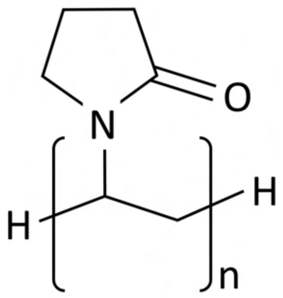

Figure 16: Chemical structure of PVP

For the functionalization of the nanoparticles, I used PVP K-30 with a molar mass of $M_W \sim 400000$ u (Roth) following a procedure described by Kim et al. [17]. First, I added 160 mg PVP to 20 ml of each AuNS solution and sonicated the mixture for 30 minutes. I then centrifuged the solution at $\sim 12000g$ for 30 minutes in 1.5 ml Eppendorf tubes to separate the coated nanoparticles from the remaining chemicals. After removing the supernatant solution with a 5 ml syringe, I carefully collected the colored liquid settling at the bottom of the tubes and stored the highly concentrated PVP-capped AuNS in the fridge until further use.

In spectroscopy, the LSPR peaks are slightly shifted towards higher wavelengths after the coating process and the absorbance increases compared to the untreated equivalent (cf. figure (17)). This can be taken as an indication of successful ligand exchange, as the change in the chemical environment of the nanoparticle increases the refractive index at the surface and causes the plasmon resonance to shift toward red [11, 18, 34, 40]. As described by Piella et al., the shift in the plasmon resonance is smaller for larger particles than for smaller ones [29].

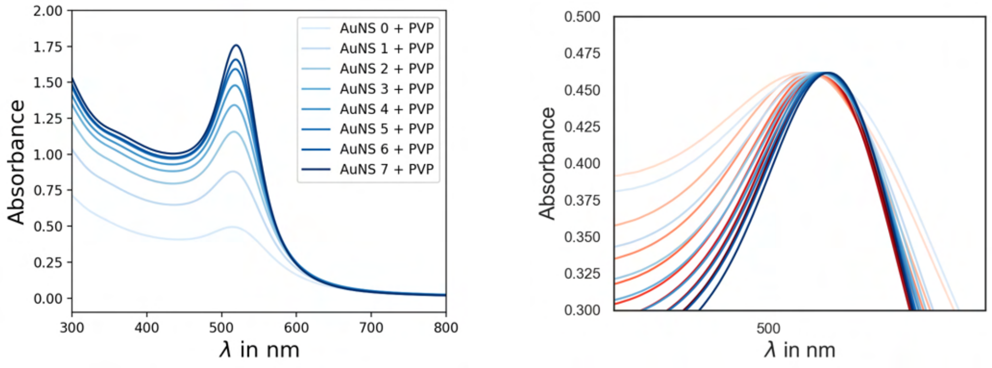

(a)

(b)

Figure 17: **(a)** Spectra of the PVP-coated AuNS
**(b)** Section of the spectra normalized to the LSPR peak: uncoated (red) and coated with PVP (blue)

## 4.2 Catalytic Measurements

I prepared the reaction solution according to the procedure described by Kim et al. [17], mixing 1.5 ml of the AuNS solution and 0.5 ml of $K_3Fe(CN)_6$ (3 mM) ($\sim$ 99%, Sigma Aldrich) in a UV-compatible glass-cuvette. I then deoxygenized the solution for 20 min by purging it with nitrogen gas under continuous stirring with a magnetic stirrer.

After twenty minutes, the exchange of $O_2$ for $N_2$ was completed, and I added 262 $\mu$l of ethanol to the solution for a total concentration of 2 M before quickly sealing the cuvette with parafilm to prevent evaporation. To be able to measure the reaction temperature of the solutions, I used a thermo-cuvette with a sheated temperature sensor in the lid (cf. figure (18)).

Figure 18: $HAuCl_4$, $K_3FeCN_6$ and Ethanol in cuvette

After recording a UV-Vis spectrum of the unreacted solution, I placed the cuvette into the laser beam that was adjusted to 1 W and focused on a circular beam with a diameter of 1 cm with the help of a power meter. I had to ensure that the temperature sensor did not obstruct the incident light beam in the spectroscopy or when illuminated by the laser.

During the experiment, the cuvette heated up noticeably under the illumination of the laser. Although it seems unlikely that only the heating of the bulk solution under CW irradiation is responsible for the catalysis [43], the role of the reaction temperature must be taken into consideration.

### 4.2.1 Influence of Temperature

To investigate the influence of temperature on the reaction rate, I externally heated the cuvette with a heating plate during laser excitation under continuous stirring. I illuminated the sample at the same laser power for 50 minutes at time intervals of 10 min and carried out UV-Vis spectroscopy after every time interval. Figures (34a, c, e) in appendix **C** show the spectra and conversion from $Fe^{3+}$ to $Fe^{2+}$ for three different temperatures.

As can be seen in figure (19), the reaction rates increase significantly at higher temperatures. The heating process took a certain amount of time, and the temperature settings were difficult to control, so an average value had to be calculated over the temperatures measured during the reaction. The temperature increased by up to 10°C within the 10-minute reaction, so an uncertainty of ±5°C was applied to the data.

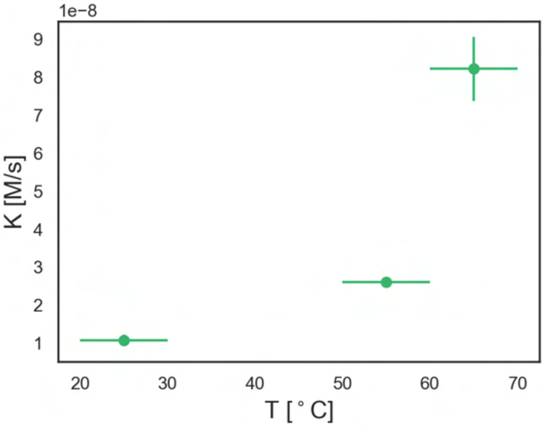

Figure 19: Calculated reaction rates $K$ for different temperatures $T$

The solution temperature plays an essential role. The experiments must be performed at comparable solution temperatures to allow comparability of reaction rates. The high-intensity laser light allows the solution to heat up even without a heating plate. Furthermore, since scattering is negligible for small particles, it must be ensured that all particle samples absorb the incident light to the same extent. Due to the previously described manufacturing process, the number of gold atoms increases with ascending particle size. As the maximal absorbance can be assumed to be a measure of the total gold volume in solution (cf. formula (6)), the LSPR resonances of the different samples must be identical. I diluted the AuNS solutions with small amounts of water and compared the maximum absorbance with a target value by UV-Vis spectroscopy (cf. figure (20a)).

An absorbance value at the LSPR-peak of $Abs_{LSPR} \sim 1.2$, measured on the peak between 500 and 600 nm could be achieved for samples 'AuNS 1-7' (cf. figure (20b). Since the seed solution (AuNS 0) contains the lowest number of gold atoms and could not be concentrated by centrifugation, I had to concentrate on the larger nanoparticles for the catalysis experiments.

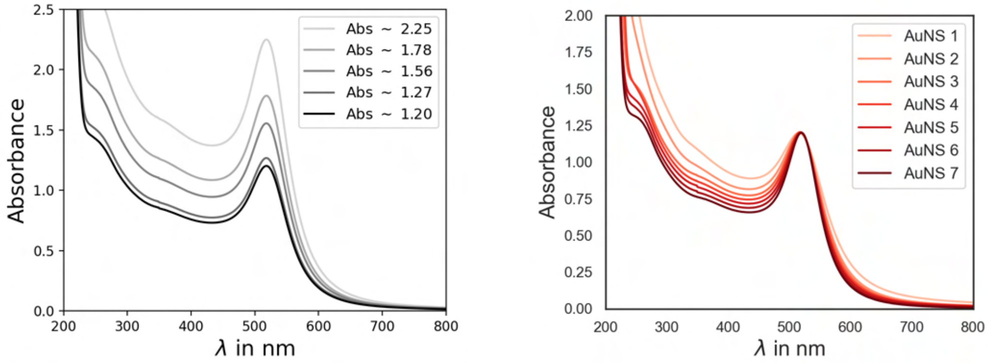

(a)

(b)

Figure 20: **(a)** Spectra of one AuNS sample in different stages of dilution **(b)** Spectra of the AuNS samples with adjusted concentrations

### 4.2.2 Influence of Size

I now carried out the described measurements with the nanoparticle samples '1-7' without external heating but with an extended reaction time of 90 min. The determined reaction rates with their respective errors are shown in figure (21) as a function of the sample enumeration (a) and the sizes determined from the TEM images (b). The error in the x-direction of (21b) corresponds to the standard deviation determined from the size distribution (cf. table (2)). In a second series, the samples were only illuminated for 50 min at 10 min intervals, with five nanoparticle samples produced the same way. The sizes of the nanoparticles for the second series have not been determined, so due to the identical preparation procedure, I adopted the size distribution from series 1.

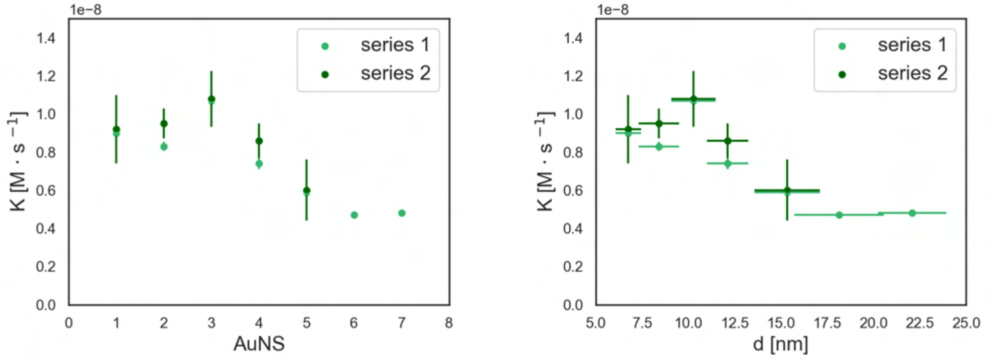

(a) (b)

Figure 21: Reaction rates $K$ depending on the sample name **(a)** and the nanoparticle diameter $d$ **(b)** for two different series carried out

Three of the five measurement points in the two series are located close to each other, with the measurements of series 2 consistently slightly higher than that of series 1. A clear formation of a maximum reaction rate for the nanoparticle sample 'AuNS 3' with an average diameter of 10.3 nm is observed in both series. With increasing size, the reaction rate steadily decreases and reaches a minimum at a size of about 18-20 nm before slightly increasing again. It would be interesting to verify if this upward trend continues for longer measurements with larger particles. A lower reaction rate can be observed in the first measurement series for the 8 nm particles than for the smallest sample. However, the second series shows a steady downward trend from a nanoparticle size below 10 nm. The error bars are much smaller in the first series of measurements because ten values were recorded this time to document the reaction rate instead of six measuring points.

To determine whether the solutions heat up to the same extent, I recorded the solution temperature at the beginning and the end of the 10-minute laser irradiation periods for each reaction series with a temperature probe. Figure (22) shows the temperature change in each excitation step over the entire reaction time for the samples 'AuNS 1-7'.

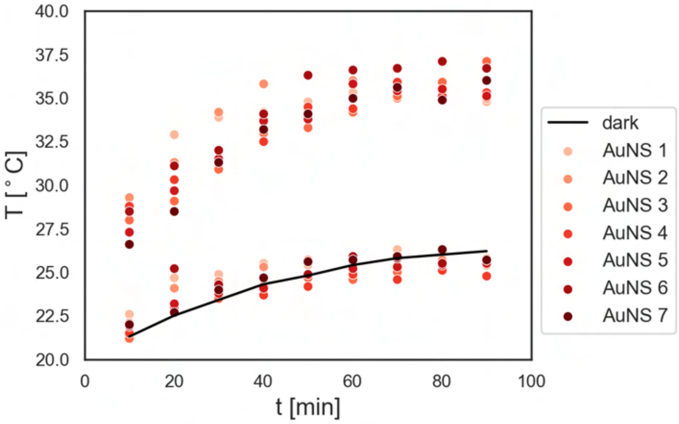

Figure 22: Measured sample temperatures in the beginning (lower point cloud) and at the end (upper point cloud) of the 10 min illumination time and measured temperatures of a sample stirred in the dark for 90 min (black line)

During illumination, the solution temperature increases by about 5-10 K, with the degree of heating increasing as the experiment progresses.

A control experiment carried out in the dark suggests that the additional temperature rise observed in all samples is due to the inevitable heating of the hot plate by the stirring motion. After subtracting this background heating, a temperature increase of about 5-10 K can be attributed to laser excitation.

### 4.2.3 Control Experiments

In order to investigate the influence of laser irradiation on a reaction, I placed one sample of 'AuNS 3' with ferricyanide and ethanol in a darkened container under constant stirring, and performed a spectroscopy every 25 minutes for 200 min (cf. figure (23a)). The calculated reaction rate of $9 \cdot 10^{-10} \frac{\mathrm{M}}{\mathrm{s}}$ is significantly lower than the reaction under light exposure ($\sim 10^{-8} \frac{\mathrm{M}}{\mathrm{s}}$, cf. figure (21)).

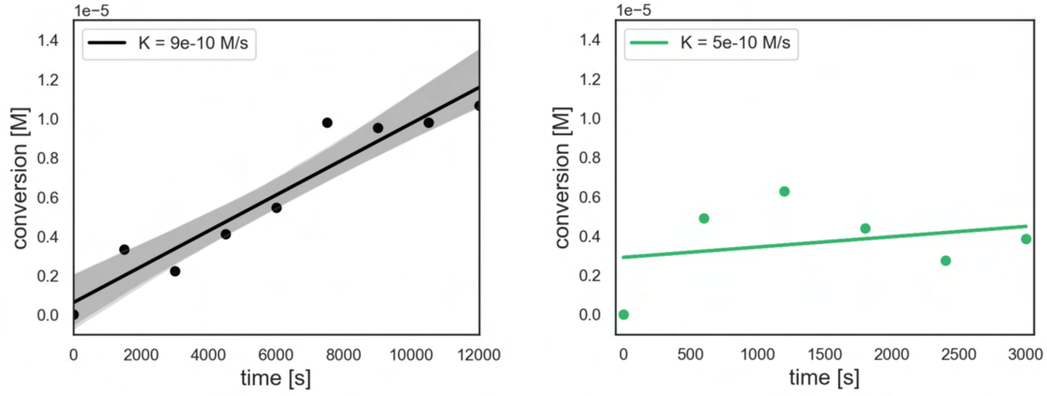

(a) (b)

Figure 23: $Fe^{3+}$ to $Fe^{2+}$ conversion at room temperature **(a)** with AuNS in the dark **(b)** without AuNS under excitation

To examine the influence of irradiation at a higher reaction temperature, I repeated the experiment carried out at 65 °C without the influence of the laser. As can be seen in figure (24), the conversion of $Fe^{3+}$ to $Fe^{2+}$ is reduced from $8.22 \cdot 10^{-8} \frac{\mathrm{M}}{\mathrm{s}}$ to $3.22 \cdot 10^{-8} \frac{\mathrm{M}}{\mathrm{s}}$.

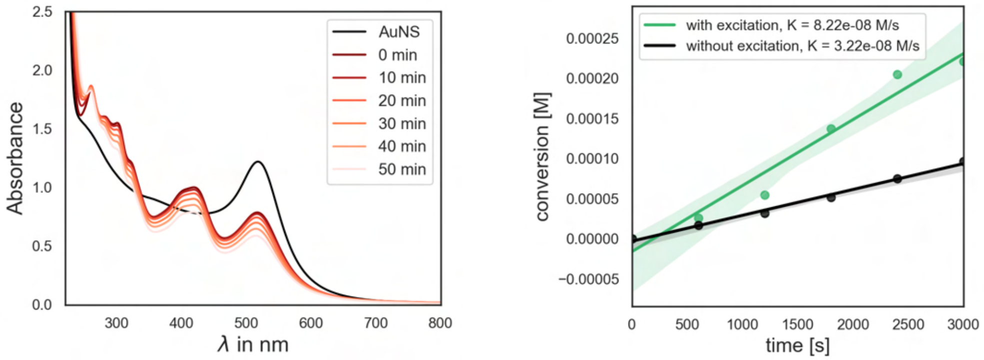

(a) (b)

Figure 24: (a) Spectroscopy of a reaction at 65 °C carried out in the dark (b) Calculated conversions at 65 °C with and without excitation

To ensure that the reaction does not occur without the addition of nanoparticles, I used 1.5 ml of deionized water instead of the 1.5 ml AuNS for one measurement, while I left the rest of the experimental design unchanged. As a result, no significant reaction can be observed under laser excitation without the addition of nanoparticles (cf. figure (23b)).

# 5 Discussion

The reaction rates measured at room temperature are of the same order of magnitude as those documented by Kim et al. [17] and can be increased up to tenfold by increasing the solution temperature to 65°C (cf. figure (19)).
At low reaction temperatures, the reaction rate of ferricyanide reduction is approximately an order of magnitude lower than that measured under the influence of light (cf. figure (23)). This observation is consistent with the measurements reported by Kim et al. [16, 17] at a temperature of 40 °C. As the reaction temperature increases, the differences between the reaction rates with and without light decrease. At a temperature of 65 °C, the reaction rate in the dark is reduced by only half compared to the laser-driven one. This behavior was not reported by Kim and coworkers.
Since no reaction is detectable without the addition of nanoparticle solution, the catalysis can indeed be attributed to the influence of nanoparticles. This confirms the measurements performed by Kim et al. [17].
The temperature measurements taken during the size-dependent series show the same degree of heating for all samples, and no correlation with the reaction rate can be observed (cf. figure (22)). With a concentration normalized to the absorption of the solution, nanoparticle size does not affect the degree of heating of the reaction solution. It is still possible that briefly generated high temperatures at the surface of the nanoparticles during relaxation ('local heating') affect the reaction rate [4].
These results are most likely attributed to many different effects that might influence each other. This chapter discusses comparable experiments that have been conducted on the size dependence of nanoparticle-driven catalytic reactions. Finally, the changes observed in the plasmon resonance of the nanoparticles during the reaction are briefly addressed, and the mechanism of the charge transfer and the role of the capping agent will be discussed.

## 5.1 Explanatory approaches

Most of the papers dealing with size-dependent photocatalysis remain rather vague in analyzing the results. Whenever explanatory approaches are made, the transferability of the experiment is often questionable since other materials are used, or different reactions are examined.

In their studies on glucose oxidation with uncoated ('naked') gold nanoparticles, Comotti et al. conclude that the plasmon-induced catalytic activity increases with decreasing diameter. Between 3 and 6 nm, the reaction rate follows a $\frac{1}{r}$ dependence until it decreases drastically at a diameter of 6 nm the reaction rate. [7]

The experiments performed by Tsunoyama et al. with PVP-coated nanoclusters show a similar increase in the reaction rate for the oxidation of p-hydroxybenzyl alcohol. The smallest size investigated here is 1.3 nm, but they suggest that nanoparticles with a diameter of one nanometer or less can be expected to have a further increased catalytic activity [36, 38]. Both experiments were performed without the influence of light, so the catalytic ability of the nanoparticles cannot be attributed to plasmonic effects. The documented $\frac{1}{r}$ dependence suggests a relationship with the surface area to volume ratio. The same effect should also be observed on nanoparticle diameters larger than those studied in the two experiments. However, this does not explain the reproducible peak in the reaction rate that occurs at a nanoparticle size of 10 nm.

A simulation by Manjavacas et al. calculates the efficiency of hot charge carrier generation in nanoparticles ranging in size from 5 to 25 nm. The simulations are designed for silver nanoparticles and therefore neglect the possibility of hot-carrier generation from the d-band. However, at the excitation wavelength of 532 nm, the intraband transitions predominate over the interband transitions [17], so the described mechanism is still applicable to the present experiment. The theoretical model calculates the generation rates and energies of hot charge carriers for different particle sizes and lifetimes $\tau$ of the excited states. With increasing diameter, a higher number of hot charge carriers with lower energies are generated. Figure (25) shows the hot charge carrier generation-efficiency $N_{\epsilon}(\tau)$ as a function of the particle size for different threshold energies according to the calculations carried out.

For short lifetimes $\tau$ of the excited states, more hot charge carriers are generated for smaller nanoparticles (black and blue line). For higher lifetimes between $\tau = 0.5$ ps and $\tau = 1$ ps, charge carrier generation increases sharply with increasing diameter before reaching a peak at 10 nm and decreasing again (red and yellow line). The peak formed in figure (21) might be attributed to the exceptionally efficient generation of energetic electrons. Also, it can be concluded from the results of this work in connection with the simulations of Manjavacas et al. that the excited intraband transitions in the nanoparticles have a comparatively long lifetime.

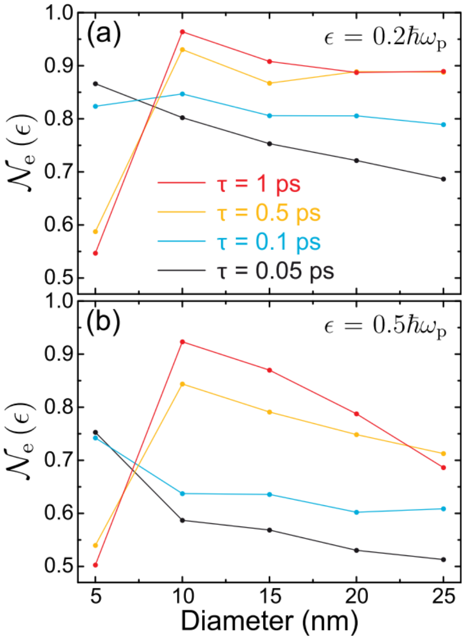

Figure 25: Efficiency $N_{\epsilon}(\tau)$ of hot electron generation per excited plasmon with energies larger than **(a)** 20 % and **(b)** 50 % of the plasmon energy $E_p = \hbar\omega_p$ (Reprinted with permission from [26], Copyright 2014, ACS)

The results of the size-dependent measurements shown in figure (21) could be a superposition of the two effects described: The catalytic ability of the nanoparticles depends on the available surface area and therefore has a $\frac{1}{r}$ dependence at constant gold volume. Under the influence of light, a particularly large number of energetic electrons are generated at a nanoparticle size of 10 nm, so the reaction rate is exceptionally high at this point.

## 5.2 Absorption at Laser Resonance

To keep the absorbed power the same for all samples, the nanoparticle samples were normalized to the same height of their LSPR peak prior to reaction. As can be seen in figure (20b), the plasmon band becomes wider and wider as the particle size decreases, resulting in a continuous increase in absorption at the laser resonance at 532 nm. Since the size distribution of the samples averages 11.4 % with no apparent trend (cf. table (2)), this broadening effect can be attributed primarily to the increased damping of the plasmon on the particle surface with decreasing size [11].

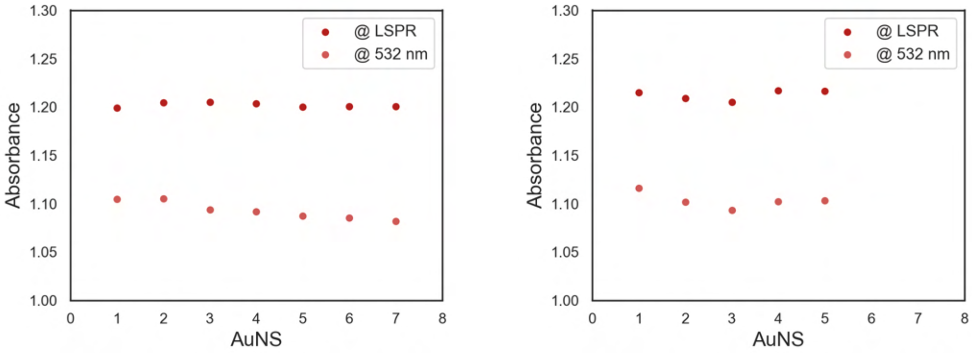

(a) series 1

(b) series 2

Figure 26: Absorbance values at LSPR position and at laser resonance ($\lambda = 532$ nm) in the samples with adjusted concentrations for the two series respectively

Figure (26) shows the absorbance values determined at the LSPR resonance and the laser resonance for the two series, respectively. While relatively strong fluctuations are visible in the second series, more attention was paid to the correct adjustment of the particle concentration in the first round. Here, the absorbance of the plasmon peak barely changes over the different sizes, indicating a similar number of gold atoms in the solution. For the absorption at 532 nm, a slight upward trend towards smaller diameters can be observed. The energy introduced into the system results essentially from the absorption of the laser light, so an increase in the absorption of the solution at laser resonance may increase the reaction rate and thus also contribute to the trends observed in figure (21).

The determined absorption values at the LSPR resonances are slightly higher for the second series of measurements than for series 1 (cf. figure (21)). If the samples have the same particle diameters, this translates into a different concentration of nanoparticles. The influence of nanoparticle concentration on the reaction rate remains to be investigated. However, the slightly increased reaction rate of series 2 compared to series 1 may indicate that an increase in the number of particles available for catalysis also increases the reaction rate.

## 5.3 Observations on the LSPR band

In the measurements carried out at different temperatures (figures 34a, c, e in appendix **C**), a blue shift of the LSPR-peak can be observed along with a decrease in the absorbance. At a temperature of 65 °C, the solution even loses its color completely within 50 min (cf. figure (27)). Not only the molecule $Fe^{3+}$, but also the nanoparticles seem to undergo a reaction that has not yet been investigated.

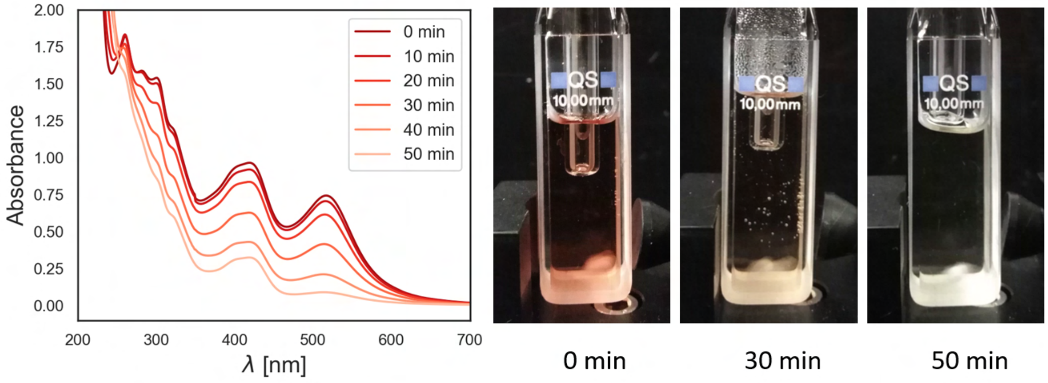

Figure 27: Spectra and photos of a sample reacted at 65 °C

Although they do not address it in detail, Kim et al. seem to have observed the decrease in plasmon resonance: To remove the changing background of the nanoparticle spectrum from the data over time, the spectra are normalized to the decreasing height of the LSPR resonance (cf. formula (7)).

To quantify the change in the LSPR peak of the gold nanoparticles, I carried out a similar calculation as previously used for the molecules:

For the calculation of the absorbance coefficient $\alpha_\lambda$, I used the spectra of the uncoated particles (cf. figure (13)). After correcting the data by subtracting the absorbance values at 800 nm from the spectra, I measured the absorbance at the LSPR-peak $Abs_\lambda$. Each molecule of $HAuCl_4$ produces one gold ion as a result of the reduction by sodium citrate, so the concentration of gold ions can be calculated from the previously described recipe (cf. appendix **B**).

| **AuNS** | $\lambda$ **[nm]** | $Abs_\lambda$ | $\alpha_\lambda$ $[\frac{1}{\mathbf{M}}]$ |
|---|---|---|---|
| **1** | 512 | 0.79 | 2911.4 |
| **2** | 514 | 1.05 | 3131.9 |
| **3** | 515 | 1.24 | 3288.1 |
| **4** | 516 | 1.38 | 3394.5 |
| **5** | 517 | 1.51 | 3573.3 |
| **6** | 517 | 1.59 | 3674.9 |
| **7** | 518 | 1.68 | 3817.0 |

Table 3: Measured LSPR position $\lambda$ with respective absorbance $Abs_\lambda$ and calculated absorbance coefficient $\alpha_\lambda$

Since the LSP resonance is directly dependent on the number of available electrons and all gold ions are expected to aggregate into particles, the gold concentration can then be used to determine the absorbance coefficients $\alpha_\lambda$ using the formula (8) (cf. table 3)).

With formula (9), I calculated the conversion of the nanoparticles. At room temperature, the reaction rates qualitatively follow those of $Fe^{3+}$ to $Fe^{2+}$ (cf. figure (28a).

The reaction rates calculated for higher temperatures are shown in appendix **C** and summarized in figure (28b). The conversion is comparatively small at room temperature but increases sharply at higher temperatures, even exceeding the reaction rates of $Fe^{3+}$.

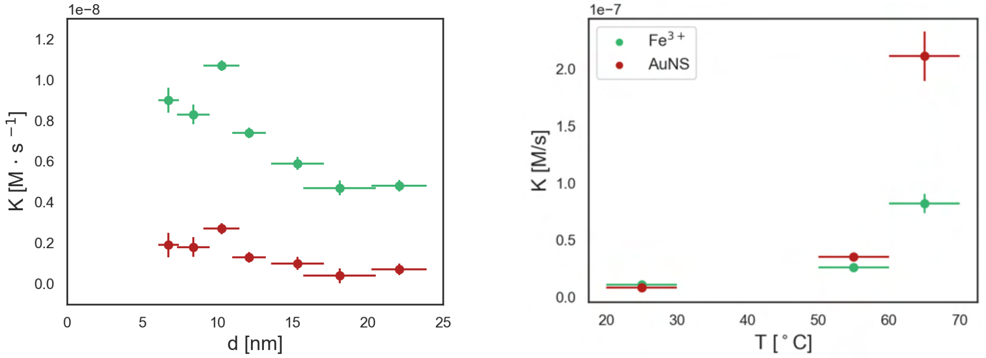

(a)

(b)

Figure 28: Calculated reaction rates $K$ for Fe$^{3+}$ and AuNS
**(a)** for different samples at room temperature
**(b)** for 'AuNS 3' at different temperatures $T$

If all LSPR peaks of figure (9) are normalized to one (arbitrary) height, a gradual shift towards higher energies is visible (cf. figure 29). Generally, a higher reaction rate is accompanied by a stronger plasmon resonance shift (cf. appendix **B**).

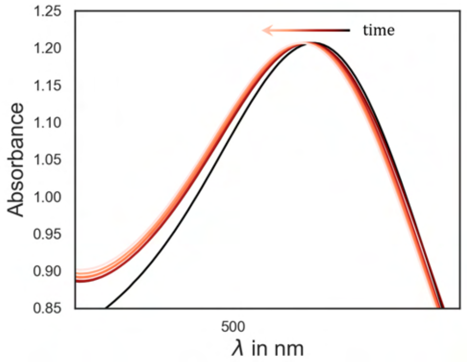

Figure 29: LSPR-resonance shifts as the reaction process progresses at 55 °C (figure (9a) normalized on peak height))

Whether the particles dissolve during the reaction or whether the charge transfer leads to a reduced plasmonic response of the positively charged nanoparticles - as both simulations and ellipsometric measurements carried out by Goldmann et al. might suggest [11] - is yet to be determined. When addressing this question, it is necessary to understand the principles underlying the charge transfer from the nanoparticles to the adjacent molecules.

## 5.4 Nature of Charge Transfer

A central question is where the charge carriers originally come from that the nanoparticles provide to the reaction. Does ethanol cause the nanoparticle to become negatively charged before electrons are transferred to $K_3Fe(CN)_6$ (10 a) or does ethanol serve to discharge the positively charged particle (10 b)?

$$\begin{aligned}
\textbf{(a)}\quad & \mathrm{NP} + \mathrm{EtOH} \rightarrow \mathrm{NP}^- + \mathrm{C_2H_5O} \bullet + \mathrm{H}^+ \\
& \mathrm{NP}^- + \mathrm{K_3Fe(CN)_6^{4-}} \rightarrow \mathrm{NP} + \mathrm{K_3Fe(CN)_6^{3-}} \\
\textbf{(b)}\quad & \mathrm{NP} + \mathrm{K_3Fe(CN)_6^{4-}} \rightarrow \mathrm{NP}^+ + \mathrm{K_3Fe(CN)_6^{3-}} \\
& \mathrm{NP}^+ + \mathrm{EtOH} \rightarrow \mathrm{NP} + \mathrm{C_2H_5O} \bullet + \mathrm{H}^+
\end{aligned} \tag{10}$$

Non-radiative recombination of electron-hole pairs in metals takes place on a time-scale of ∼ ps [16, 24, 43]. So most of the photogenerated electrons that would potentially be available for a reaction recombine with their respective holes before charge transfer could take place [1, 8, 17, 35, 37].

According to Kim et al., some holes in the d-band, created by optical excitation, are immediately filled with electrons provided by the hole scavenger ethanol, charging the particle and raising the Fermi level by up to 240 meV, which facilitates an electron transfer to ferricyanide.

For a successful charge transfer, the electrons must overcome the activation barrier $\Delta H$ (cf. figure (30)). The electron energy required for this process can be provided either thermally or by absorption of the incident light. The subsequent reorganization of the shell causes the system to fall into a low energy state, and the reaction is complete. Under the influence of light, the energy level of the reactant is raised due to the additional energy input into the system, which simplifies overcoming the activation barrier. [16]

Under optimal conditions, up to $10^3$ additional electrons can be added to a single 12 nm particle, increasing the electron density by about 13 % [16, 43]. According to the calculations given in appendix **B**, one nanoparticle with a diameter of 13 nm has around $5 \cdot 10^6$ electrons, and hence the number of electrons changes by only 0.2 %. However, this does not yet take into account that predominantly the conduction electrons and, to a small extent, the electrons of the d-band can contribute to the reaction.

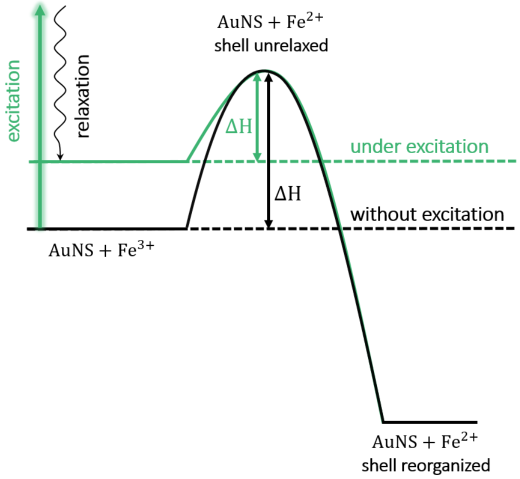

Figure 30: Illustration of photocatalysis of $Fe^{3+}$ to $Fe^{2+}$ under and without laser excitation (cf. [16])

According to the conception of Kim et al., the nanoparticles can only provide electrons to the reaction if they have previously been negatively charged by accepting additional electrons [16]. It would then seem unlikely that the nanoparticles can become positively charged at all, let alone permanently hold a strong positive charge and, as a result, lose their plasmon resonance. On the other hand, whether the nanoparticles become positively or negatively charged during the reaction may depend on the respective rates of reaction and counter-reaction.

## 5.5 The Role of PVP

When considering the chemical reaction, the role of the capping agent remains a significant source of uncertainty.

Kim et al. suggest that PVP acts as an electron donor in the absence of a hole scavenger [16] which can be confirmed by calculations carried out by Okumura et al. [27]. It seems possible that the oxidation of PVP at high reaction rates causes the bonds to the gold surface to loosen, thus decreasing the protective function of PVP. In this case, however, the nanoparticles would coagulate with visible precipitation at the bottom of the cuvette instead of dissolving.

Haesuwannakij et al. show that the density of the protective PVP structure depends on the chain length of the polymer and the size of the nanoparticles involved (cf. figure (31)) [12]. According to this logic, the comparatively short polymers used in this work form a looser structure on smaller nanoparticles, increasing the likelihood of ferrocyanide being close to the gold surface. In addition, Zhai et al. describe the formation of an electrical layer enabled by PVP, which allows the stabilization of hot electrons at the surface of the nanoparticle [44].

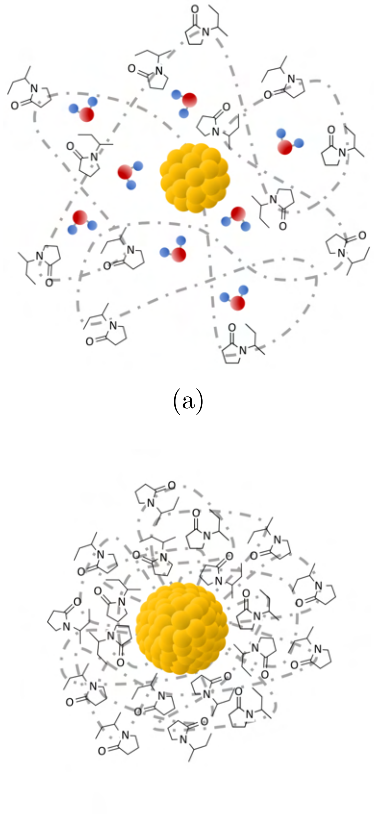

(a)

(b)

Figure 31: Different capping regimes of PVP:
**(a)** PVP with short chain length on small nanoparticles
**(b)** Longer PVP-chains on larger particles (cf. [12])

# 6 Conclusion and Outlook

I was able to show that the size of the nanoparticles used in this work significantly affects their catalytic ability. The reduction of ferricyanide driven by PVP-coated gold nanospheres shows a maximum reaction rate for particle diameters of 10 nm. Overall, smaller nanoparticles catalyze the reaction more efficiently than larger ones, although the trend might be reversed at sizes larger than 20 nm. I used nanoparticles with sizes between 7 and 22 nm in this work. A repetition of the experiment for lower and higher sizes is possible and beneficial for a better understanding of the reaction.

The influence of temperature on the reaction rate is undoubtedly large but cannot yet be quantified. By heating the solution, the reaction rate achievable in the dark can be significantly increased until it exceeds the conversions measurable at room temperature under the influence of light.

The nanoparticles also react during catalysis, which can be observed in spectroscopy as a decrease and blue shift of the LSPR. What happens to the nanoparticles and which mechanisms are responsible remains to be investigated. The capping agent could play an important role in answering this question, so it may be instructive to repeat the reaction with uncoated nanoparticles or experiment with other polymer chain lengths and capping agents.

The studies conducted in this work to increase the efficiency of photocatalytic reactions leave much room for further experimentation. For example, this work has not paid attention to excitation-related parameters such as excitation wavelength and spot size.

For a more meaningful statement about the altered reaction kinetics, the activation energy must be calculated, which is equal to the slope of a linear approximation of the measurement results in Arrhenius representation [16]. In addition, an altered experimental design requires precise temperature control, taking into account the differences between the solution temperature and the temperature at the particle surface.

# References

[1] M. Ahlawat, D. Mittal, and V. Govind Rao. Plasmon-induced hot-hole generation and extraction at nano-heterointerfaces for photocatalysis. *Communications Materials*, 2(1):114, 2021.

[2] U. Aslam, V. G. Rao, S. Chavez, and S. Linic. Catalytic conversion of solar to chemical energy on plasmonic metal nanostructures. *Nature Catalysis*, 1(9):656–665, 2018.

[3] R. Becker and W. Döring. Kinetische behandlung der keimbildung in übersättigten dämpfen. *Annalen der Physik*, 416(8):719–752, 1935.

[4] M. L. Brongersma, N. J. Halas, and P. Nordlander. Plasmon-induced hot carrier science and technology. *Nature nanotechnology*, 10(1):25–34, 2015.

[5] P. H. Camargo and E. Cortés. *Plasmonic Catalysis*. Wiley, 2021.

[6] S. Carregal-Romero, J. Pérez-Juste, P. Hervés, L. M. Liz-Marzán, and P. Mulvaney. Colloidal gold-catalyzed reduction of ferrocyanate (iii) by borohydride ions: A model system for redox catalysis. *Langmuir*, 26(2):1271–1277, 2010.

[7] M. Comotti, C. Della Pina, R. Matarrese, and M. Rossi. The catalytic activity of "naked" gold particles. *Angewandte Chemie International Edition*, 43(43):5812–5815, 2004.

[8] E. Contreras, C. Palacios, I. B. Becerril-Castro, and J. M. Romo-Herrera. *Plasmon Induced Photocatalysts for Light-Driven Nanomotors*, volume 12 of *Micromachines*. 2021.

[9] G. FRENS. Controlled nucleation for the regulation of the particle size in monodisperse gold suspensions. *Journal of Physics: Condensed Matter*, 241(105):20–22, 1973.

[10] R. S. Geonmonond, da Silva, Anderson G. M., T. S. Rodrigues, I. C. de Freitas, R. A. Ando, T. V. Alves, and P. H. C. Camargo. Addressing the effects

of size-dependent absorption, scattering, and near-field enhancements in plasmonic catalysis. *ChemCatChem*, 10(16):3447–3452, 2018.

[11] C. Goldmann, R. Lazzari, X. Paquez, C. Boissière, F. Ribot, C. Sanchez, C. Chanéac, and D. Portehault. Charge transfer at hybrid interfaces: Plasmonics of aromatic thiol-capped gold nanoparticles. *ACS Nano*, 9(7):7572–7582, 2015.

[12] S. Haesuwannakij, T. Kimura, Y. Furutani, K. Okumura, K. Kokubo, T. Sakata, H. Yasuda, Y. Yakiyama, and H. Sakurai. The impact of the polymer chain length on the catalytic activity of poly(n-vinyl-2-pyrrolidone)-supported gold nanoclusters. *Scientific reports*, 7(1):9579, 2017.

[13] W. Haiss, N. T. K. Thanh, J. Aveyard, and D. G. Fernig. Determination of size and concentration of gold nanoparticles from uv−vis spectra. *Analytical Chemistry*, 79(11):4215–4221, 2007.

[14] P. Hervés, M. Pérez-Lorenzo, L. M. Liz-Marzán, J. Dzubiella, Y. Lu, and M. Ballauff. Catalysis by metallic nanoparticles in aqueous solution: model reactions. *Chemical Society Reviews*, 41(17):5577–5587, 2012.

[15] N. R. Jana, L. Gearheart, and C. J. Murphy. Seed-mediated growth approach for shape-controlled synthesis of spheroidal and rod-like gold nanoparticles using a surfactant template. *Advanced Materials*, 13(18):1389–1393, 2001.

[16] Y. Kim, D. Dumett Torres, and P. K. Jain. Activation energies of plasmonic catalysts. *Nano letters*, 16(5):3399–3407, 2016.

[17] Y. Kim, J. G. Smith, and P. K. Jain. Harvesting multiple electron-hole pairs generated through plasmonic excitation of au nanoparticles. *Nature chemistry*, 10(7):763–769, 2018.

[18] C. Kinnear, H. Dietsch, M. J. D. Clift, C. Endes, B. Rothen-Rutishauser, and A. Petri-Fink. Gold nanorods: controlling their surface chemistry and complete detoxification by a two-step place exchange. *Angewandte Chemie (International ed. in English)*, 52(7):1934–1938, 2013.

[19] S. K. Kulkarni. *Nanotechnology: Principles and practices.* Capital Publishing Company and Springer, New Delhi and Cham, third edition edition, 2015.

[20] V. K. La Mer. Nucleation in phase transitions. *Industrial & Engineering Chemistry*, 44(6):1270–1277, 1952.

[21] V. K. LaMer and R. H. Dinegar. Theory, production and mechanism of formation of monodispersed hydrosols. *Journal of the American Chemical Society*, 72(11):4847–4854, 1950.

[22] G. J. Lauth and J. Kowalczyk, editors. *Einführung in die Physik und Chemie der Grenzflächen und Kolloide.* Springer Berlin Heidelberg, Berlin, Heidelberg, 2016.

[23] S. Leydecker, editor. *Nanomaterialien: in Architektur, Innenarchitektur und Design.* Birkhäuser Basel, Basel, 2008.

[24] S. Link and M. A. El-Sayed. Size and temperature dependence of the plasmon absorption of colloidal gold nanoparticles. *The Journal of Physical Chemistry B*, 103(21):4212–4217, 1999.

[25] S. Link and M. A. El-Sayed. Optical properties and ultrafast dynamics of metallic nanocrystals. *Annual Review of Physical Chemistry*, 54(1):331–366, 2003.

[26] A. Manjavacas, J. G. Liu, V. Kulkarni, and P. Nordlander. Plasmon-induced hot carriers in metallic nanoparticles. *ACS nano*, 8(8):7630–7638, 2014.

[27] M. Okumura, Y. Kitagawa, and T. Kawakami. Dft calculations for the heterojunction effect between metal clusters and the stabilizer molecules. *International Journal of Quantum Chemistry*, 110(15):2903–2911, 2010.

[28] J. H. Perepezko and M. J. Uttormark. Undercooling and nucleation during solidification. *ISIJ International*, 35(6):580–588, 1995.

[29] J. Piella, N. G. Bastús, and V. Puntes. Size-controlled synthesis of sub-10-nanometer citrate-stabilized gold nanoparticles and related optical properties. *Chemistry of Materials*, 28(4):1066–1075, 2016.

[30] J. Polte. Fundamental growth principles of colloidal metal nanoparticles – a new perspective. *CrystEngComm*, 17(36):6809–6830, 2015.

[31] V. Prasad, D. Semwogerere, and E. R. Weeks. Confocal microscopy of colloids. *Journal of Physics: Condensed Matter*, 19(11):113102, 2007.

[32] S. Siahrostami, G.-L. Li, V. Viswanathan, and J. K. Nørskov. One- or two-electron water oxidation, hydroxyl radical, or h2o2 evolution. *The Journal of Physical Chemistry Letters*, 8(6):1157–1160, 2017.

[33] F. Stete. *Gold at the nanoscale.* PhD thesis, University of Potsdam, 2021.

[34] Y. Tao, J. Yang, L. Chen, Y. Huang, B. Qiu, L. Guo, and Z. Lin. Dialysis assisted ligand exchange on gold nanorods: Amplification of the performance of a lateral flow immunoassay for e. coli o157:h7. *Microchimica Acta*, 185(7):350, 2018.

[35] T. Tsukuda, H. Tsunoyama, and H. Sakurai. Aerobic oxidations catalyzed by colloidal nanogold. *Chemistry – An Asian Journal*, 6(3):736–748, 2011.

[36] H. Tsunoyama, N. Ichikuni, and T. Tsukuda. Microfluidic synthesis and catalytic application of pvp-stabilized, approximately 1 nm gold clusters. *Langmuir*, 24(20):11327–11330, 2008.

[37] H. Tsunoyama, H. Sakurai, and T. Tsukuda. Size effect on the catalysis of gold clusters dispersed in water for aerobic oxidation of alcohol. *Chemical Physics Letters*, 429(4):528–532, 2006.

[38] H. Tsunoyama and T. Tsukuda. Magic numbers of gold clusters stabilized by pvp. *Journal of the American Chemical Society*, 131(51):18216–18217, 2009.

[39] J. Turkevich, P. C. Stevenson, and J. Hillier. A study of the nucleation and growth processes in the synthesis of colloidal gold. *Discussions of the Faraday Society*, 11(0):55–75, 1951.

[40] L. Vigderman, P. Manna, and E. R. Zubarev. Quantitative replacement of cetyl trimethylammonium bromide by cationic thiol ligands on the surface of gold nanorods and their extremely large uptake by cancer cells. *Angewandte Chemie (International ed. in English)*, 51(3):636–641, 2012.

[41] F. Wang, Y. Dai, J. Zhao, Q. Li, and B. Zhang. Effect of size on fracture and tensile manipulation of gold nanowires. *Journal of Nanoparticle Research*, 16(12):2752, 2014.

[42] S. Yu, A. J. Wilson, J. Heo, and P. K. Jain. Plasmonic control of multi-electron transfer and c-c coupling in visible-light-driven co2 reduction on au nanoparticles. *Nano letters*, 18(4):2189–2194, 2018.

[43] S. Yu, A. J. Wilson, G. Kumari, X. Zhang, and P. K. Jain. Opportunities and challenges of solar-energy-driven carbon dioxide to fuel conversion with plasmonic catalysts. *ACS Energy Letters*, 2(9):2058–2070, 2017.

[44] Y. Zhai, J. S. DuChene, Y.-C. Wang, J. Qiu, A. C. Johnston-Peck, B. You, W. Guo, B. DiCiaccio, K. Qian, E. W. Zhao, F. Ooi, D. Hu, D. Su, E. A. Stach, Z. Zhu, and W. D. Wei. Polyvinylpyrrolidone-induced anisotropic growth of gold nanoprisms in plasmon-driven synthesis. *Nature materials*, 15(8):889–895, 2016.

# A Illustration of the Synthesis Process

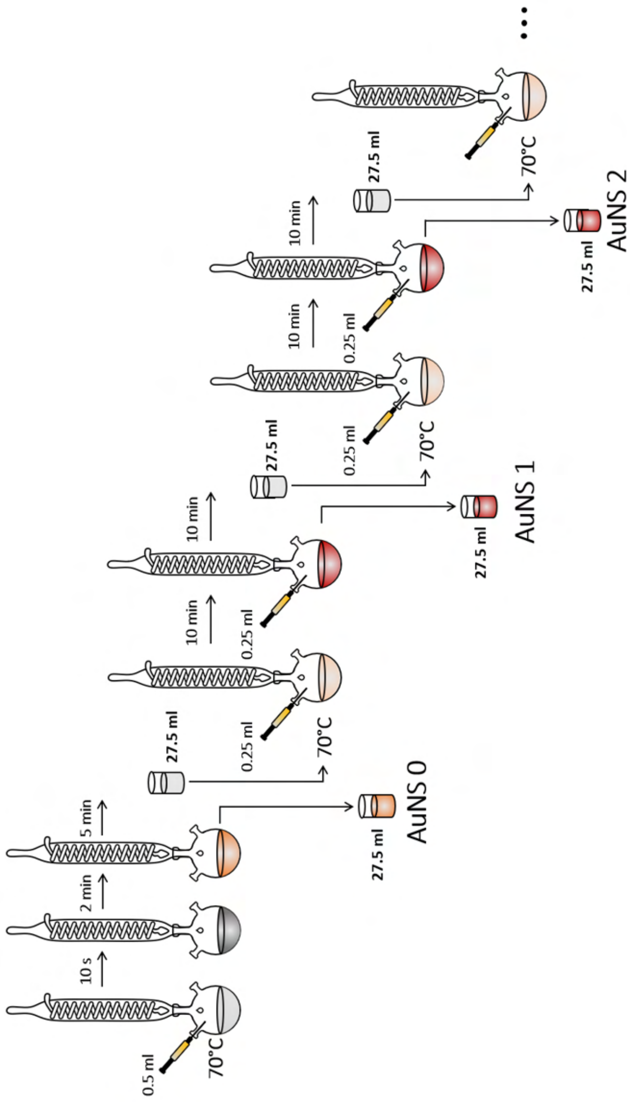

Figure 32: Illustration of the recipe described by Piella et al. (cf. ESI to [29])

# B Calculations on Au-Concentration

The seed solution ('AuNS 0') is composed of 0.5 ml of HAuCL$_4$ (25 mM), 75 ml sodiumcitrate and 0.05 ml of tannic acid. For the gold concentration in the initial solution $c_0$ we calculate

$$\begin{aligned} c_0 &= \frac{V^{Au}}{V^{add}} \cdot c^{Au} \\ &= \frac{0.5\,\text{ml}}{(0.5 + 0.05 + 75)\,\text{ml}} \cdot 25\,\text{mM} \\ &= 0.165\,\text{mM} \end{aligned} \tag{11}$$

In every growth step, $V^{ext} = 27.5$ ml are extracted from the solution and replaced by 27.5 ml sodium citrate and a total of 0.5 ml of HAuCL$_4$ (25 mM). In the added solution the gold concentration is

$$\begin{aligned} c^{add} &= \frac{V^{Au}}{V^{ges}} \cdot c^{Au} \\ &= \frac{0.5\,\text{ml}}{(0.5 + 27.5)\,\text{ml}} \cdot 25\,\text{mM} \\ &= 0.446\,\text{mM} \end{aligned}$$

The resulting solution is composed of the initial solution volume left in the flask and the added volume:

$$V_i^{ges} = V_{i-1}^{left} + V^{add}$$

The new gold concentration $c_i$ can be calculated as follows:

$$c_i = \frac{V^{add}}{V_i^{ges}} \cdot c^{add} + \frac{V^{left}}{V_i^{ges}} \cdot c_{i-1} \tag{12}$$

An estimate of the number of gold atoms per particle requires some calculations. Due to the double assignment of some formula characters, a double indexing is used in the following. The lower index refers to the numbering of the described nanoparticle sample 'AuNS 0-7".

|  |  | **present** | **extracted** | **left** | **added** |  |
|---|---|---|---|---|---|---|
| **AuNS** | $c_i$ | $V_i^{ges}$ | $V^{ext}$ | $V_i^{left}$ | $c^{add}$ | $V^{add}$ |
| **0** | 0.165 mM | 75.55 ml | 27.50 ml | 48.05 ml | 0.446 mM | 28 ml |
| **1** | 0.270 mM | 76.05 ml |  | 48.55 ml |  |  |
| **2** | 0.336 mM | 76.55 ml |  | 49.05 ml |  |  |
| **3** | 0.378 mM | 77.05 ml |  | 49.55 ml |  |  |
| **4** | 0.405 mM | 77.55 ml |  | 50.05 ml |  |  |
| **5** | 0.423 mM | 78.05 ml |  | 50.55 ml |  |  |
| **6** | 0.434 mM | 78.55 ml |  | 51.05 ml |  |  |
| **7** | 0.441 mM | 79.05 ml |  | 51.55 ml |  |  |

Table 4: Concentrations of goldions in the different steps of the synthesis (cf. figure (32)) with concentrations calculated with formula (12)

As shown in figure 33, a gold crystal can be described as a face-centered cubic Bravais lattice (fcc) with a monatomic base. Since none of the 14 atoms have their full volume inside the cell, $8 \cdot \frac{1}{8} + 6 \cdot \frac{1}{2} = 4$ atoms can be counted per unit cell. With a lattice constant of $a = 0.408$ nm [41] we get a volume of $V^{cell} = 0.06791$ nm$^3$ for one cubic cell.

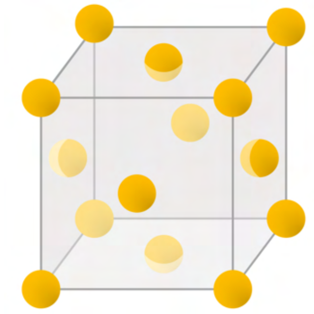

Figure 33: Model of a fcc-gold crystal with monoatomic base

Based on these considerations and depending on the size of the initial nanoparticles 'AuNS 0', the sizes of the nanoparticles of all other samples can now be calculated.

The concentrations $c_i$ listed in table (4) can be converted into absolute numbers $N_i^{Au}$ of gold atoms in solution using the Avogadro constant $N_A$. Since the concentration is given in M, i.e. $\frac{\text{mol}}{\text{l}}$, the number must be normalized to the volume of the solution:

$$N_i^{Au} = N_A \cdot c_i \cdot \frac{V_i^{ges}}{1000 \text{ ml}} \tag{13}$$

From the TEM images, a radius of $r_0 = 2.5$ **nm** can be deduced for the nanoparticles in solution 'AuNS 0' so every particle has a volume of

$$V_0^{NP} = \frac{4}{3}\pi r_0^3 = 65.45 \text{ nm}^3$$

If each unit cell consisting of four atoms has a volume of $V^{cell} = 0.06791 \text{ nm}^3$, the initial nanoparticles in 'AuNS 0' are composed of

$$n_0 = \frac{65.45 \text{ nm}^3}{0.06791 \text{ nm}^3} \cdot 4 = 3855$$

gold atoms.

According to formula (13), the gold concentration in 'AuNS 0' corresponds to a total number of

$$N_0^{Au} = N_A \cdot 0.165 \text{ mM} \cdot \frac{75.55 \text{ ml}}{1000\text{ml}} = 7.53 \cdot 10^{18}$$

gold atoms so the number of nanoparticles in the 'AuNS 0' solution would be

$$N_0^{NP} = \frac{N_0^{Au}}{n_0} = 1.95 \cdot 10^{15}$$

As one fraction of the nanoparticle solution is extracted in each growth step, the number of nanoparticles in solution decreases according to

$$N_i^{NP} = \frac{V_i^{left}}{V_i^{ges}} \cdot N_{i-1}^{NP}$$

In the present reaction, the gold atoms added in the growth step do not form new particles but attach to the existing nanoparticles. The numbers of atoms per nanoparticle of every solution $n_i$ can therefore be calculated by dividing the total number of atoms in solution $N_i^{Au}$ by the number of nanoparticles present in every sample $N_i^{NP}$. The resulting diameter $d_i$ of the nanoparticles can then be calculated using the formula (14). Table (5) lists the sizes calculated in this way, which remain within the confidence interval of the TEM-based size measurements except for the last sample.

$$\begin{aligned} n_i &= \frac{N_i^{Au}}{N_i^{NP}} \\ \Rightarrow d_i &= 2 \cdot \sqrt[3]{\frac{3}{4\pi} \frac{n_i \cdot 0.069\ \mathrm{nm}^3}{4}} \end{aligned} \tag{14}$$

| **AuNS** | $n$ | $d$ **[nm]** | $a$ **[nm]** | $n_{e^-}$ |
|---|---|---|---|---|
| **0** | 3855 | 5 | 338.21 | $3.05 \cdot 10^5$ |
| **1** | 9918 | 6.89 | 393.65 | $7.83 \cdot 10^5$ |
| **2** | 19407 | 8.61 | 457.61 | $1.53 \cdot 10^6$ |
| **3** | 34187 | 10.40 | 531.31 | $2.70 \cdot 10^6$ |
| **4** | 57113 | 12.35 | 616.14 | $4.51 \cdot 10^6$ |
| **5** | 92537 | 14.50 | 713.66 | $7.31 \cdot 10^6$ |
| **6** | 147070 | 16.92 | 825.65 | $1.16 \cdot 10^7$ |
| **7** | 230722 | 19.66 | 954.13 | $1.82 \cdot 10^7$ |

Table 5: Calculations on the number of atoms per particle $n$, diameter $d$, interparticle distance $a$ and number of electrons per particle $n_{e^-}$

# C Reaction Rates at different Temperatures

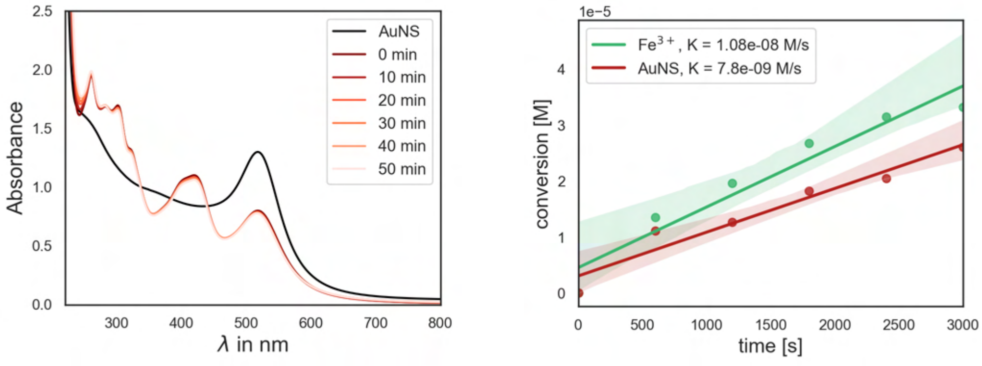

(a) Spectroscopy at 25 °C (b) Reaction rate $K$ at 25 °C

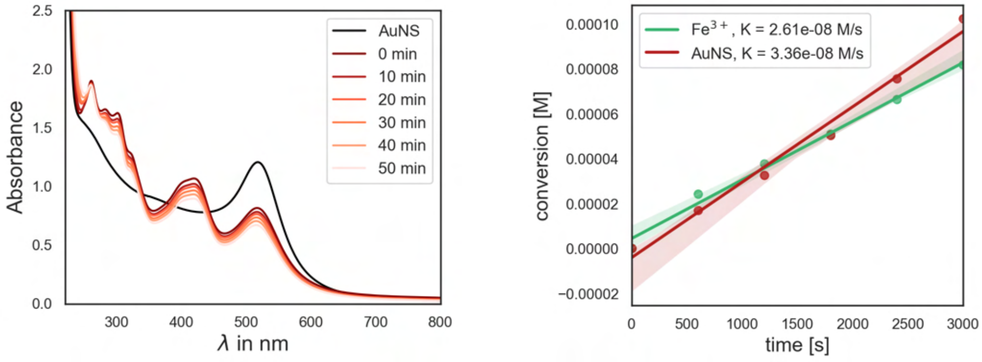

(c) Spectroscopy at 55 °C (d) Reaction rate $K$ at 55 °C

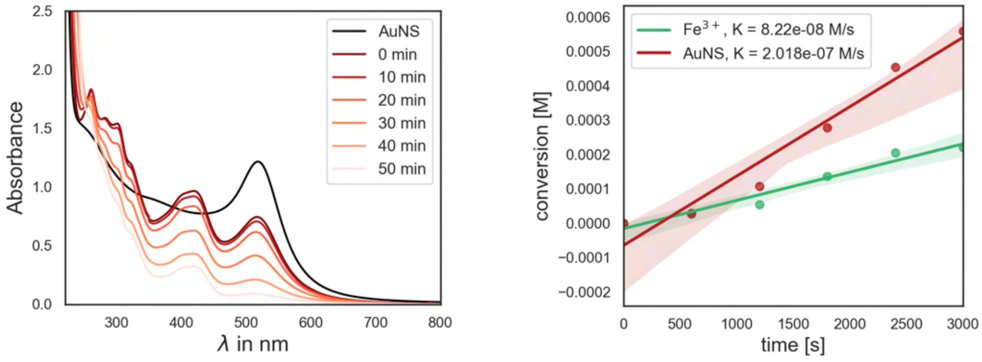

(e) Spectroscopy at 65 °C (f) Reaction rate $K$ at 65°C

Figure 34: Observations for different temperatures $T$ under excitation Reaction rate $K$ corresponds to the slope of the linear fit